



Geochemistry and petrology of listvenite in the Samail ophiolite, Sultanate of Oman: Complete carbonation of peridotite during ophiolite emplacement

Elisabeth S. Falk*, Peter B. Kelemen

Lamont-Doherty Earth Observatory, Columbia University, Palisades, NY 10964, USA

Received 16 May 2014; accepted in revised form 14 March 2015; available online 20 March 2015

Abstract

Extensive outcrops of listvenite—fully carbonated peridotite, with all Mg in carbonate minerals and all Si in quartz—occur along the basal thrust of the Samail ophiolite in Oman. These rocks can provide insight into processes including (a) carbon fluxes at the “leading edge of the mantle wedge” in subduction zones and (b) enhanced mineral carbonation of peridotite as a means of carbon storage. Here we examine mineralogical, chemical and isotopic evidence on the temperatures, timing, and fluid compositions involved in the formation of this listvenite. The listvenites are composed primarily of magnesite and/or dolomite + quartz + relict Cr-spinel. In some instances the conversion of peridotite to listvenite is nearly isochemical except for the addition of CO₂, while other samples have also seen significant calcium addition and/or variable, minor addition of K and Mn. Along margins where listvenite bodies are in contact with serpentinized peridotite, talc and antigorite are present in addition to carbonate and quartz. The presence of antigorite + quartz + talc in these samples implies temperatures of 80–130 °C. This range of temperature is consistent with dolomite and magnesite clumped isotope thermometry in listvenite (average $T = 90 \pm 15$ °C) and with conventional mineral-water oxygen isotope exchange thermometry (assuming fluid $\delta^{18}\text{O}$ near zero). CO₂-bearing fluids responsible for the formation of listvenite were likely derived from underlying calcite-bearing metasediment during emplacement of the ophiolite. An internal Rb–Sr isochron from one listvenite sample yields an age of 97 ± 29 Ma, consistent with the timing of emplacement of the ophiolite over allochthonous sediments of the Hawasina group, and autochthonous sediments of the Arabian continental margin. Most of the initial ⁸⁷Sr/⁸⁶Sr values in the listvenite, ranging from 0.7085 to 0.7135, are significantly higher than seawater values and consistent with values measured in the underlying metasediments. While constraints on the pressure of listvenite formation are lacking, the moderate temperatures suggest that listvenites formed at relatively shallow depths in the subduction zone, making release of carbonate-saturated pore-water due to compaction of subducted sediment or low-pressure phase transitions of hydrous minerals, such as clays, probable sources of the CO₂-bearing fluid. Carbonate dissolution from subducted sediments and transfer of CO₂ to the mantle wedge to form listvenites may be an important process in forearc hydrothermal systems. Additionally, the presence of listvenites demonstrate that peridotite carbonation reactions can proceed to completion on large scales, suggesting that *in situ* mineral carbonation of peridotite may offer a viable solution for carbon storage.

© 2015 Elsevier Ltd. All rights reserved.

1. INTRODUCTION

* Corresponding author at: MS#8, Woods Hole Oceanographic Institution, Woods Hole, MA 02543-1539, USA.

E-mail address: efalk@whoi.edu (E.S. Falk).

Listvenite (*sensu stricto*) is a fuchsite–quartz–carbonate assemblage produced by alteration of ultramafic rocks (Halls and Zhao, 1995), but the term has been broadly

applied to include many other carbonate-rich alteration products of ultramafic rocks. In this paper, we use the term to refer to rocks composed almost entirely of quartz + magnesite and/or dolomite, formed by CO₂-metasomatism of peridotite. Listvenite deposits initially attracted attention for their association with gold mineralization and other economically-valuable hydrothermal deposits (Rose, 1837), but more recently have been highlighted as a natural analog to mineral carbon storage (Hansen et al., 2005; Kelemen et al., 2011; Beinlich et al., 2012).

Other carbonated peridotite lithologies can be found throughout the Samail ophiolite. Previous studies have highlighted the geologically rapid ongoing formation of carbonate veins and travertine deposits in association with low-temperature alteration of peridotite as a promising example of the potential for enhanced *in situ* mineral carbonation of peridotite to provide an effective method of permanent carbon storage (e.g., Kelemen and Matter, 2008). While ongoing low-temperature carbonation processes provide useful information about carbonation rates and the propagation of carbonate veins, listvenites provide an opportunity to understand the conditions under which complete carbonation of peridotite can be achieved. Other highly carbonated products of peridotite alteration, such as magnesite-talc “soapstone” are also exist in Oman, and some comparisons between partially carbonated peridotite lithologies and listvenite in Oman can be found in the [Electronic Supplement, Section S.1](#).

The presence of listvenite near the base of the Samail ophiolite has been noted by several researchers (Glennie et al., 1974; Stanger, 1985; Villey et al., 1986; Wilde et al., 2002; Nasir et al., 2007; Kelemen et al., 2011), but there has been no consensus on a model for the formation of listvenite in Oman. Referred to as alternatively as “Amqat,” birbirite, silicified serpentinite, listwaenite, or listwanite, these rocks have been proposed to have formed by leaching of magnesium under tropical weathering conditions in the late Tertiary (Glennie et al., 1974), reaction with warm groundwater during Paleogene faulting (Stanger, 1985; Wilde et al., 2002), and reaction with sediment-derived fluids during emplacement of the ophiolite (Kelemen et al., 2011). We present geochemical data from Oman listvenites to provide constraints on the timing, temperature, fluid composition, and fluid sources for listvenite formation.

We collected listvenite and nearby metasediment and serpentinized peridotite from a large antiform comprising a ridge crest just north of Wadi Mansah, 12 km southeast of Fanjah. A list of sample locations and descriptions can be found in [Supplementary Table S1](#). The location of our field area within the Samail ophiolite is shown in [Fig. 1](#), and a geologic map of this locality is presented in [Fig. 2](#). In Wadi Mansah, listvenite forms 10 to ~200 m thick bands roughly parallel to banding in the host peridotite (pictured in [Fig. 3](#)). Beneath the listvenites and their host peridotite are minor amphibolites, greenschist facies metabasalts and chert, plus more extensive sections of metasedimentary phyllites containing quartz, calcite, clinocllore, illite and muscovite. These lithologies are part of the metamorphic sole of the ophiolite (Villey et al., 1986). In turn, beneath

the metamorphic sole are diagenetically modified sediments of the Hawasina group (Villey et al., 1986).

Our field area falls within the region of detailed mapping of the “Amqat” occurrence described by Stanger (1985) and is located within a few kilometers of the listvenite outcrops described by Wilde et al. (2002). However, many of the listvenite samples we collected at these localities are not consistent with previous descriptions of listvenite from this region. Lithologies interpreted as listvenites in previous studies from this area include highly silicified serpentinite containing only minor dolomite and/or calcite (Glennie et al., 1974; Stanger, 1985; Wilde et al., 2002; Nasir et al., 2007), and carbonate-dominated listvenite composed of dolomite and/or calcite with accessory fuchsite, chlorite, quartz, barite and oxides (Nasir et al., 2007). The listvenite in Wadi Mansah differs from samples described in these previous studies in the predominance of magnesite. The magnesite + quartz assemblage that typifies listvenite at the Wadi Mansah locality reflects carbonation of peridotite with relatively little change to the bulk composition beyond the addition of CO₂, whereas other listvenite bodies in Oman are dominated by dolomite and calcite (e.g., Stanger, 1985; Wilde et al., 2002; Nasir et al., 2007).

2. METHODS

2.1. Compositional analyses

The mineralogical and elemental compositions of samples were studied by petrographic microscope, powder X-ray diffraction (XRD), X-ray fluorescence (XRF), and electron microprobe. Powdered samples were analyzed by XRD using a Panalytical X’Pert powder X-ray diffractometer at Lamont-Doherty Earth Observatory and peaks for constituent minerals were identified using MacDiff (Petschick, 2001) and Match! software (Brandenburg and Putz, 2009). Whole rock major and trace element composition were determined by XRF at the Washington State University GeoAnalytical Lab, where loss on ignition (LOI), primarily due to volatilization of H₂O + CO₂, was also measured (<http://environment.wsu.edu/facilities/geo-lab/>). Back-scattered electron images and major element composition of phases in polished thin sections were obtained using a 5-spectrometer Cameca SX-100 electron microprobe located at the American Museum of Natural History in New York. Carbonate and silicate mineralogy of listvenite samples, identified by optical petrography, XRD and EMPA, are included in [Table 1](#). Bulk rock compositions by XRF are shown in [Supplementary Table S4](#). Summary electron microprobe data are presented in [Supplementary Tables S7–S12](#).

2.2. Sr isotopes and isotopic dating

Sr isotopic analyses were completed at Lamont-Doherty Earth Observatory, using a VG Sector 54 multi-collector thermal ionization mass spectrometer (TIMS). Bulk Sr isotope ratios were measured in listvenites and underlying allochthonous metasedimentary and metavolcanic rocks

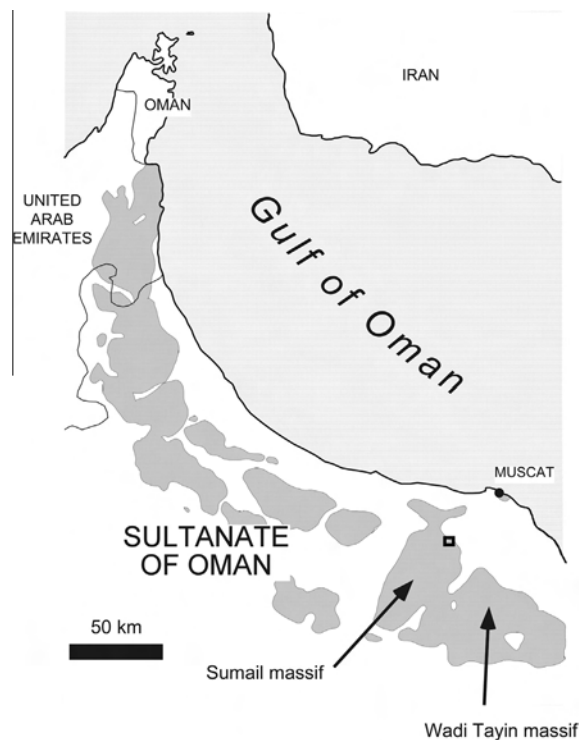


Fig. 1. Map of the Samail ophiolite in Oman and the UAE, after Lippard et al. (1986). Small rectangle indicates approximate location of geologic map of Wadi Mansah in Fig. 2.

from Wadi Mansah. Mineral separation for determination of an internal Rb–Sr mineral isochron in sample OM10-26 was partially achieved by magnetic separation of sieved grains liberated by self-fragmentation under high voltage (Selfrag). Although the fine-grained nature of these rocks and variable mineral compositions prevented complete separation of minerals, eight fractions with variable proportions of quartz, magnesite, and fuchsite were obtained and analyzed for Sr isotopic ratios. Rb:Sr ratios for Rb–Sr dating were analyzed by inductively coupled plasma mass spectrometry (ICP-MS) measured on a VG PlasmaQuad Excell ICPMS. Summary Sr isotopic data are presented in Supplementary Tables S13 and S14.

2.3. Carbonate clumped isotopes

The carbonate clumped isotope paleothermometer is based on the temperature-dependent abundance of ^{13}C – ^{18}O bonds in carbonate minerals relative to a stochastic distribution. The extent of “clumping” of ^{13}C and ^{18}O is quantified using the variable $\Delta 47$, which measures the excess of mass-47 CO_2 (primarily $^{13}\text{C}^{18}\text{O}^{16}\text{O}$) relative to the abundance expected for stochastic distribution of the same bulk isotopic composition (Wang et al., 2004). $\Delta 47$ values are positively correlated with $1/T^2$, where T is the temperature of carbonate formation in Kelvin (Ghosh et al., 2006). Unlike conventional stable isotope thermometers, clumped isotope thermometry does not depend on the isotopic composition of the fluid from which the carbonate

was precipitated, making it useful in ancient terrestrial and low-temperature hydrothermal environments (Eiler, 2011).

Clumped isotopic data were obtained on magnesite, dolomite, and calcite from listvenite and underlying allochthonous metasediments from Wadi Mansah. All samples were analyzed at the California Institute of Technology (Caltech), over two sessions in 2011 and 2012. To validate the application of clumped isotope thermometry to magnesite, magnesite samples formed at known temperatures were also analyzed. These included synthetic magnesite samples grown at temperatures of 40–250 °C (Deelman, 1999; Hänchen et al., 2008; Saldi et al., 2010, 2012); natural playa magnesite from Atlin, British Columbia formed at ~ 3 –10 °C (Power et al., 2014); magnesite + quartz listvenite from Atlin, British Columbia, with fluid inclusion temperatures of 210–180 °C (Andrew, 1985; Hansen et al., 2005); and a magnesite-bearing metaperidotite from Val d’Efra, Switzerland, formed during Barrovian regional metamorphism at temperatures of 645 ± 10 °C (Ferry et al., 2005). Results of this magnesite calibration are presented in the Electronic Supplement (Supplementary Table S2, Supplementary Figure S4).

Crushed and sieved (150–250 μm) dolomite and calcite samples were reacted using the automated online extraction system described in Passey et al. (2010), wherein samples are reacted for 20 min in a common phosphoric acid bath maintained at 90 °C with continuous cryogenic trapping of evolved CO_2 followed by further automated cryogenic and GC purification. Crushed and sieved (150–250 μm) magnesite samples digested offline in phosphoric acid at 90 °C in sealed reaction vessels for 17 h. To avoid contamination from coexisting dolomite, CO_2 evolved from magnesite in the first 20 min of phosphoric acid digestion was discarded.

Carbon, oxygen, and clumped isotope ratios were measured on a Thermo Finnigan MAT 253 gas source mass spectrometer at Caltech, employing standard configurations and methods (Huntington et al., 2009; Passey et al., 2010). Heated gas samples were analyzed daily to correct for instrument nonlinearity and scale compression, allowing data to be normalized to the stochastic reference frame used for the original calibration of the clumped isotope thermometer reported in Ghosh et al. (2006). Following heated gas normalization, the empirically derived acid fractionation correction of +0.081‰ was added to $\Delta 47$ data to account for the difference between the phosphoric acid temperature of 90 °C used in this study and the phosphoric acid temperature of 25 °C used by Ghosh et al. (2006) in the original calibration (Passey et al., 2010). Clumped isotope data were converted from the Caltech reference frame to the absolute reference frame of Dennis et al. (2011) using a transfer function derived from heated gases and calcite standards analyzed over these two sessions (see Supplementary Table S3). Average clumped isotope data are presented in Table 2, and all clumped isotope data are presented in Supplementary Table S2.

2.4. Oxygen isotopes in quartz

$\delta^{18}\text{O}$ was measured in quartz separates from nine listvenite samples in which clumped isotope compositions

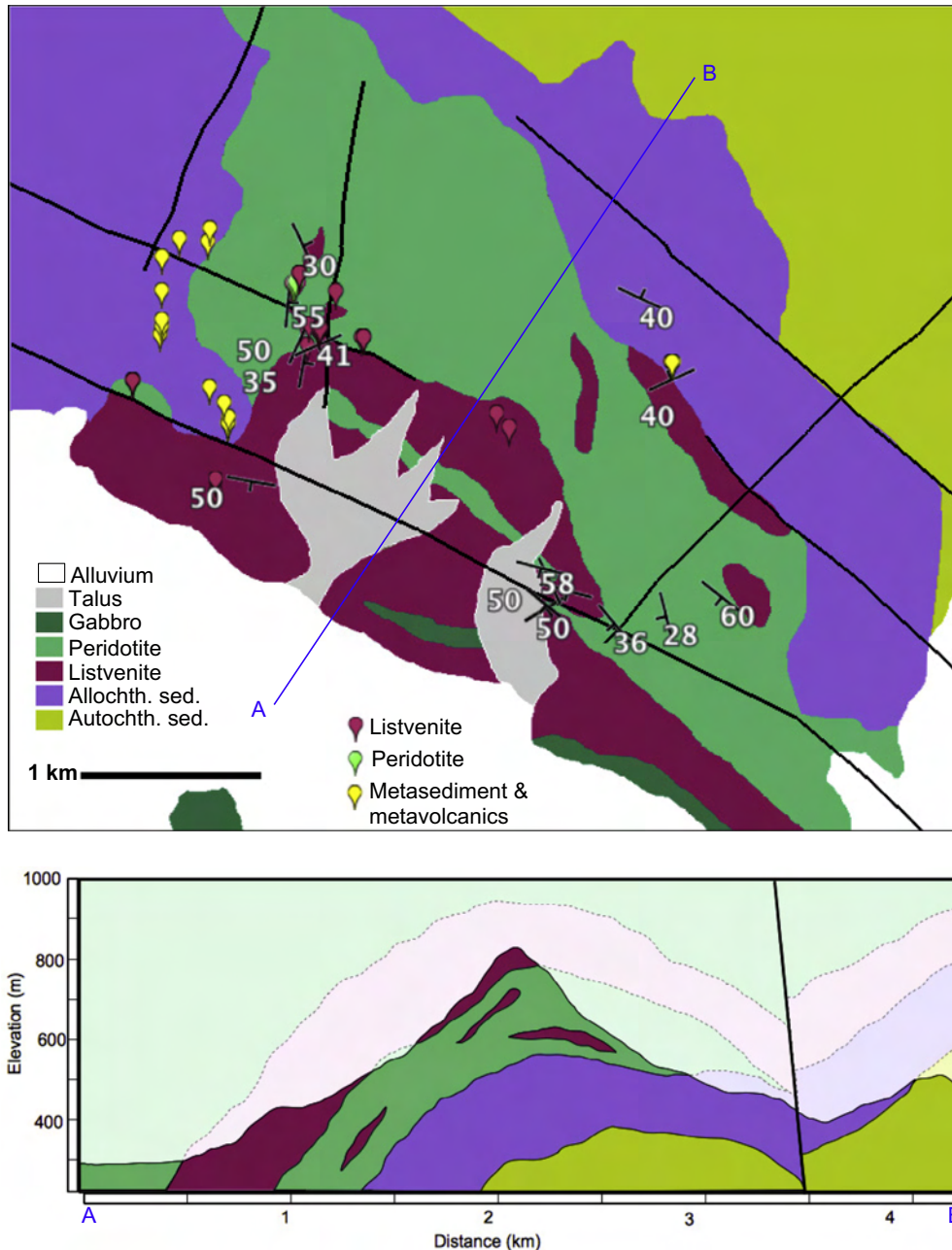


Fig. 2. Geologic map and representative cross-section of the Wadi Mansah listvenite locality, including individual sample locations (place-markers). Compiled from [Villey et al. \(1986\)](#), Google Earth data, and field observations (including hand-held GPS measurements and attitudes of compositional banding and lithological contacts). Map area is between UTM coordinates 2,582,600 m to 2,587,150 m N, and 619,900 m to 625,400 m E, in zone 40 Q. (For a full color version of this figure, the reader is referred to the web version of this article.)

were also analyzed. Crushed and sieved samples were magnetically separated, treated with HCl and oxalic acid to remove carbonate and iron oxides, and picked under a microscope. Quartz $\delta^{18}\text{O}$ measurements were performed on a Thermo MAT 253 mass spectrometer at the Earth Systems Center for Stable Isotopic Studies (ESCSIS) at Yale University, using CO_2 laser fluorination techniques. Measured sample $\delta^{18}\text{O}$ values were standardized to Gore Mountain Garnet ($\delta^{18}\text{O} = 5.8\text{‰}$ SMOW) and NBS28

quartz standards ($\delta^{18}\text{O} = 9.6\text{‰}$ SMOW). Results of quartz $\delta^{18}\text{O}$ analyses are shown in [Supplementary Table S5](#).

3. RESULTS

3.1. Mineralogy and petrology

Optical microscopy, XRD, and electron microprobe analyses reveal that our listvenite samples are

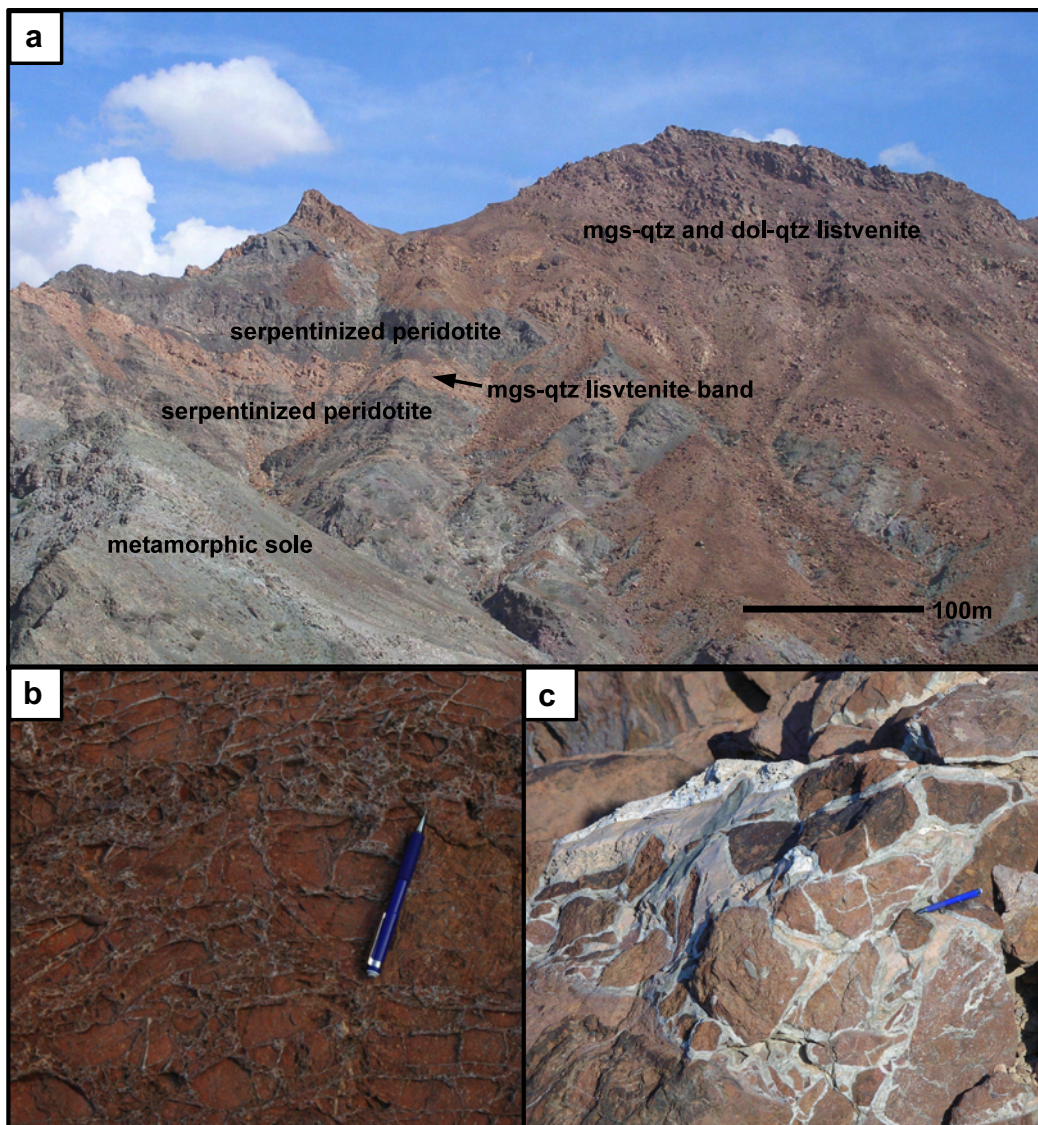


Fig. 3. Listvenite outcrops at Wadi Mansah. (a) listvenite bands enclosed in serpentinized peridotite; (b) hierarchical quartz and carbonate veins cutting finely intergrown quartz and carbonate; (c) coarse, fracture-filling dolomite on the ridge crest cutting finely intergrown dolomite and quartz.

predominantly composed of magnesite and/or dolomite + quartz, with minor Fe-oxides, relict chromian spinels and local fuchsite. In ~ 10 m thick listvenite bands occurring within partially serpentinized peridotite, the carbonate is almost exclusively magnesite (“magnesite-quartz listvenite”), while in an overlying ~ 100 m thick body of listvenite that makes up the crest of the antiform along Wadi Mansah, the carbonate is frequently dolomite (“dolomite-quartz listvenite”), though magnesite is also found in this section of the outcrop. In samples collected from “listvenite–serpentine transition zones”, antigorite \pm talc \pm chlorite are the dominant silicate phases rather than quartz. [Table 1](#) lists mineral parageneses observed in listvenites and associated rocks. Average mineral compositions from electron microprobe analyses are provided in [Supplementary Tables S7–S12](#).

In listvenites from Wadi Mansah, cross-cutting relationships suggest quartz and carbonate are coeval. Carbonate (either dolomite or magnesite) and quartz are finely intergrown, frequently down to micron scale. In addition to fine-grained matrix material, carbonate and quartz form hierarchical vein networks, in which quartz veins cut and are also cut by carbonate veins at micrometer to centimeter scales ([Figs. 4 and 5](#)). Minor dolomite and calcite occur in some magnesite-quartz listvenite as cross-cutting veins and vugs (e.g., [Fig. 4](#)). While carbonates from the active, low-temperature alteration system in Oman have <0.5 wt% FeO ([Streit et al., 2012](#)), magnesite and dolomite from Oman listvenites have a molar Mg# ($\text{Mg}/(\text{Mg} + \text{Fe})$) of ~ 0.95 on average (~ 5 wt% FeO in magnesite, ~ 2 wt% in dolomite; see [Supplementary Table S7](#)). A more detailed discussion of iron partitioning between carbonate and

Table 1
Mineral parageneses (carbonates and silicates).

Sample	Type ^a	Mgs ^b	Dol	Cc	Qtz	Serp	Ol	Tlc	Chl	Fuchs	En	Di
OM09-11	listv.	M			M					tr		
OM09-15	listv.	m	tr	tr	M							
OM09-16	listv.	M	tr		M			tr				
OM09-18	listv.	M	tr		M							
OM09-19	listv.	M	M		M							
OM09-20	listv.		M		M							
OM09-27	listv.		M		M							
OM09-28	listv.	M	m		M							
OM09-29	listv.	M	M		M							
OM09-30	listv.	m	M		m							
OM10-03	listv.	M	tr		M							
OM10-09	listv.		M									
OM10-10	listv.		M	m	M							
OM10-11	listv.		M		m							
OM10-12	listv.		M	tr	M							
OM10-14	listv.		M	m	m							
OM10-15	listv.		M	m	m							
OM10-19	listv.		M	m	M							
OM10-20	listv.		M	m	M							
OM10-24	listv.		M	M	m							
OM10-25	listv.	M	m	tr	M							
OM10-26	listv.	M		tr	M				tr	m		
OM09-12	trans.	m	m		m	M		tr	m			
OM10-02	trans.	M	m			M	tr	m				
OM10-04	trans.	M	m			M			tr			
OM10-05	trans.		tr			M						
OM09-13	s.p.					M			m			
OM09-14	s.p.					M	M				m	
OM10-01	s.p.					M	M				m	
OM10-08	s.p.					M						
OM10-06	s.p.					M	M					
OM10-07	s.p.					M	M		tr			m

M = major phase, m = minor phase, tr = trace phase.

^a Type abbrev.: listv. = listvenite, trans. = listvenite–serpentinite transition zone, s.p. = serpentinized peridotite.

^b Mineral abbrev.: mgs = magnesite, dol = dolomite, cc = calcite, qtz = quartz, serp = serpentine, ol = olivine, tlc = talc, chl = chlorite, fuchs = fuchsite, en = enstatite, di = diopside.

magnesium silicate phases in listvenites and other carbonated peridotite lithologies in Oman can be found in the Electronic Supplement ([Supplementary Figure S2](#) and related text in [Section S.1](#)).

Unlike serpentinized peridotite in Oman far from listvenites (e.g., [Boudier et al., 2010](#); [Streit et al., 2012](#)), serpentine in the listvenite–serpentinite transition zones at the margins of listvenite bodies is primarily antigorite rather than lizardite or chrysotile, though XRD suggests all three polytypes may be present in these samples. In these samples from the listvenite margin, antigorite coexists with chlorite, talc, and/or quartz ([Fig. 5c–e](#)). In contrast, serpentinites 1–3 m away from the listvenite margin are ~30–100% serpentinized, with mesh-texture lizardite and chrysotile surrounding relict olivine (“partially serpentinized peridotite”). In the listvenite–serpentinite transition zones from the listvenite margin and in partially serpentinized peridotite occurring 1–3 m away from the listvenite, serpentine has an average Mg# of ~95 ([Supplementary Table S8](#)), which is the value expected for antigorite in Fe/Mg exchange equilibrium ([Trommsdorff and Evans, 1972](#)) with local relict olivine ([Supplementary Table S9](#)), similar to

typical mantle olivine from the Samail ophiolite with an Mg# of 91 ([Hanghøj et al., 2010](#)). In some of the partially serpentinized samples near the listvenite, the mesh is defined by this Mg# ~95 serpentine, but more Fe-rich serpentine (e.g., Mg# ~85) rims or completely replaces relict olivine in the mesh cores ([Supplementary Figure S3](#)).

Iron oxides are abundant in listvenite, samples from the listvenite–serpentinite transition zones, and partially serpentinized peridotite. In the listvenite–serpentinite transition zones and in partially serpentinized peridotite, fine-grained magnetite is present in disseminated patches, irregular veins, and larger aggregates (up to 30 μm) rimming Cr-spinels. In fully carbonated listvenites, iron-rich phases include fine-grained hematite and extremely fine-grained, unidentified iron oxides/hydroxides. Fine-grained hematite (<10–20 μm) occurs as isolated needles, veinlets, rims on Cr-spinels, and subhedral-to-euhedral grains in listvenite. Electron microprobe analyses of the unidentified iron-rich phase yield average totals of ~78–88 wt% and indicate ~5 wt% SiO₂ even when the iron phase occurs within pure carbonate veins and is analyzed with a 1 μm beam diameter ([Supplementary Table S10](#)). Fe K-edge

Table 2
Averaged clumped isotope data for listvenites and associated rocks.

Sample	Session	Type	Min.	<i>n</i>	$\delta^{13}\text{C}$, ‰ PDB ^a	$\delta^{18}\text{O}_{\text{CO}_2}$, ‰ SMOW ^a	$\delta^{18}\text{O}_{\text{carb}}$, ‰ PDB ^b	$\Delta 47_{\text{ARF}}$, ‰ ^{c,d}	<i>T</i> , °C Bristow ^{e,f}
OM09-19	2011	listv.	Dol	1	0.71 ± 0.25	34.22 ± 0.05	−5.73	0.519 ± 0.032	96 + 19 /− 16
OM09-20-c	2012	listv.	Dol	2	0.99 ± 0.05	33.90 ± 0.07	−6.03	0.511 ± 0.041	101 + 27 /− 21
OM09-20-f	2012	listv.	Dol	2	0.73 ± 0.03	34.64 ± 0.04	−5.32	0.489 ± 0.024	114 + 17 /− 15
OM10-14	2012	listv.	Dol	2	−1.75 ± 0.03	28.44 ± 0.04	−11.28	0.555 ± 0.030	78 + 15 /− 13
OM10-15	2011	listv.	Dol	2	−0.30 ± 0.02	33.43 ± 0.08	−6.48	0.504 ± 0.026	104 + 17 /− 14
OM10-20	2012	listv.	Dol	2	−0.46 ± 0.05	35.09 ± 0.01	−4.89	0.552 ± 0.039	79 + 20 /− 16
OM09-11	2012	listv.	Mgs	2	0.62 ± 1.03	32.93 ± 1.13	−7.43	0.521 ± 0.045	95 + 28 /− 22
OM09-15	2012	listv.	Mgs	2	−2.39 ± 0.34	31.32 ± 0.51	−8.97	0.557 ± 0.029	77 + 14 /− 12
OM09-16	2012	listv.	Mgs	2	−0.97 ± 0.15	30.96 ± 1.16	−9.32	0.517 ± 0.041	97 + 25 /− 20
OM09-18	2012	listv.	Mgs	2	−1.61 ± 0.04	31.49 ± 0.11	−8.81	0.514 ± 0.036	99 + 23 /− 19
OM09-19	2011	listv.	Mgs	2	0.16 ± 0.12	33.86 ± 0.33	−6.53	0.560 ± 0.021	76 + 10 /− 9
OM10-03	both	listv.	Mgs	3	−2.49 ± 0.15	31.99 ± 0.25	−8.33	0.596 ± 0.019	61 + 8 /− 7
OM10-26	2011	listv.	Mgs	2	0.09 ± 0.02	34.15 ± 0.10	−6.26	0.530 ± 0.013	90 + 7 /− 6
OM10-02	2012	trans.	Mgs	1	−0.68 ± 0.04	31.90 ± 0.08	−8.42	0.570 ± 0.054	71 + 26 /− 20
OM10-04	2012	trans.	Mgs	2	−3.62 ± 0.33	32.42 ± 0.36	−7.91	0.671 ± 0.023	37 + 7 /− 6
OM11-43	2012	metased.	Cc	1	−2.50 ± 0.04	29.22 ± 0.08	−9.74	0.437 ± 0.065	155 + 84 /− 49
OM11-45	2012	metased.	Cc	1	−0.17 ± 0.04	30.08 ± 0.08	−8.91	0.442 ± 0.050	150 + 57 /− 38
OM11-48	2012	metased.	Cc	1	−0.57 ± 0.04	28.99 ± 0.08	−9.96	0.421 ± 0.063	171 + 96 /− 54
OM11-47	2012	metased.	Dol	1	−4.53 ± 0.04	30.39 ± 0.08	−9.41	0.588 ± 0.059	64 + 27 /− 20

^a For $n \geq 2$, uncertainty is one standard deviation of replicate digestions (which exceeds internal error). For $n = 1$, reported uncertainty is the greater of the internal standard deviation of all sample acquisitions or the session standard deviation of calcite standards relative to expected value.

^b Carbonate $\delta^{18}\text{O}$ values calculated from phosphoric acid digestion fractionation factors at 90 °C (Das Sharma et al., 2002).

^c Clumped data converted from Caltech reference frame to absolute reference frame of Dennis et al. (2011) using a transfer function derived from calcite standards and heated gases analyzed during both analytical session. See Supplementary Table S3.

^d Reported uncertainty is the propagated internal standard deviation over all acquisitions of each digestion (which exceeds the standard deviation of replicate digestions, though typically similar in magnitude);

^e Temperature calculated using the calcite- and dolomite-derived calibration implied by the data of Bristow et al. (2011), converted to the absolute reference frame: $\Delta 47 = 0.0012x^2 + 0.0285x + 0.245$, where $x = 10^6/T^2$. For T derived from other calibrations, see Supplementary Table S2, which includes all clumped isotope data (samples, known- T mgs, stds, HG).

^f Reported uncertainty is the 1-stdev uncertainty of $\Delta 47_{\text{ARF}}$, propagated through the temperature calculation.

X-ray absorption edge spectra (XANES) on one listvenite containing this fine-grained iron phase collected by collaborators A. Templeton and L. Mayhew at University of Colorado Boulder are unique among their large library of model compounds, but are most similar to amorphous Fe(III)-oxide microbial mat spectra from low-temperature submarine hydrothermal vents (Templeton et al., 2009; Toner et al., 2012). Thus the identity of host phase for much of the iron in listvenite remains unclear.

Relict chromian spinels are common in listvenites from Wadi Mansah, and in many cases serve as the clearest indication of a peridotite protolith in these otherwise dramatically transformed rocks. Although Cr-spinel is typically the only relict phase remaining from the protolith, even these spinels have experienced significant alteration, with relatively $MgAl_2O_4$ -rich end-members typical of Oman harzburgite present only in partially serpentinized peridotites and the least-altered cores of spinels in some listvenite samples (Supplementary Table S11). Most spinel analyses from listvenite samples have much lower Mg# (average ~30) and higher Cr# (molar $Cr/(Cr + Al)$, average ~80) than spinel from fresh Oman peridotite (average Mg# ~60 in harzburgite, ~50 in dunite; average Cr# ~50 in harzburgite, ~60 in dunite) (Hanghøj et al., 2010), as is typical for spinels

affected by hydrothermal alteration (e.g., Evans and Frost, 1975; Kimball, 1990; Mellini et al., 2005).

Fuchsite (Cr-rich muscovite) occurs in trace quantities in a few samples, and in minor quantities (roughly 5%) in only one sample, OM10-26 (Table 1). Fuchsite occurs in mm-scale bright bluish-green spots composed primarily of quartz intergrown with minor amounts of very fine-grained fuchsite. Larger fuchsite grains in OM10-26 pseudomorphically replace Cr-spinel (Supplementary Figure S6), which is not present as relicts in this sample, unlike most other samples. Fuchsite compositions in this sample trend toward the Mg# and Cr# of Cr-rich spinels in listvenites (Supplementary Figure S7).

3.2. Bulk compositions

Listvenite bulk compositions, at the cubic meter scale, generally approximate the compositions of average Oman harzburgite (Godard et al., 2000; Hanghøj et al., 2010) with addition of CO_2 and in many cases Ca. A full table of bulk rock compositions by XRF can be found in Supplementary Table S4. While other studies have noted a high degree of silicification in some Oman listvenites (e.g., Stanger, 1985; Wilde et al., 2002), we find similar numbers of samples showing silica gains and losses, with silica content least variable and most similar to Oman harzburgite in the listvenite–serpentinite transition zones and in the magnesite-quartz listvenites (Fig. 4). Mg contents and Mg# in these two types of rocks (Fig. 6a and c) are also in the range of those of Oman harzburgite. The abundance of quartz veins makes it clear that silica was mobilized in the system. The relatively high Mg-numbers of quartz-rich samples (Fig. 6c) suggest that the high proportion of silica in those samples is primarily due to addition of Si (at the hand sample scale) rather than loss of Mg. Dolomite-quartz listvenites exhibit greater compositional variability than their magnesite counterparts, and appear to have lost Mg (Fig. 6a) and gained Ca (Fig. 6b).

Volatile-free concentrations of minor and trace elements in listvenites are also broadly similar to average partially serpentinized peridotite from our mapping area and from other areas of the Samail ophiolite (Fig. 7, Supplementary Table S4), with the most notable exceptions being minor addition of potassium in most listvenites, and addition of manganese in most dolomite-bearing listvenites. Fig. 7 further illustrates the calcium gain and magnesium loss experienced by dolomite–listvenites, and also shows that volatile-free major and trace element bulk compositions of magnesite-quartz listvenites are frequently the same, within error, as average Oman harzburgite for all elements for which our XRF data can be compared with the data from Hanghøj et al. (2010). The isochemical nature of magnesite–listvenite formation during peridotite carbonation is also illustrated in selected “isocon” plots in Supplementary Figure S5.

3.3. Sr isotopic compositions

Bulk strontium isotopic ratios for listvenites and underlying allochthonous metasediments and metavolcanics are

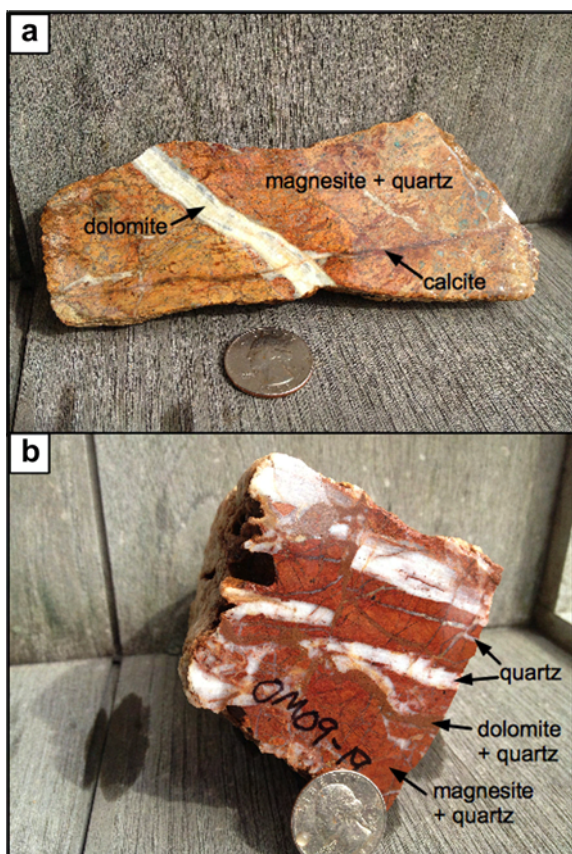


Fig. 4. Cross-cutting relationships between carbonate minerals. (a) Coarse dolomite and calcite veins cut magnesite + quartz listvenite; (b) Brown dolomite-quartz and gray quartz veins cut red magnesite + quartz and white quartz veins, OM09-19. (For interpretation of the references to color in this figure legend, the reader is referred to the web version of this article.)

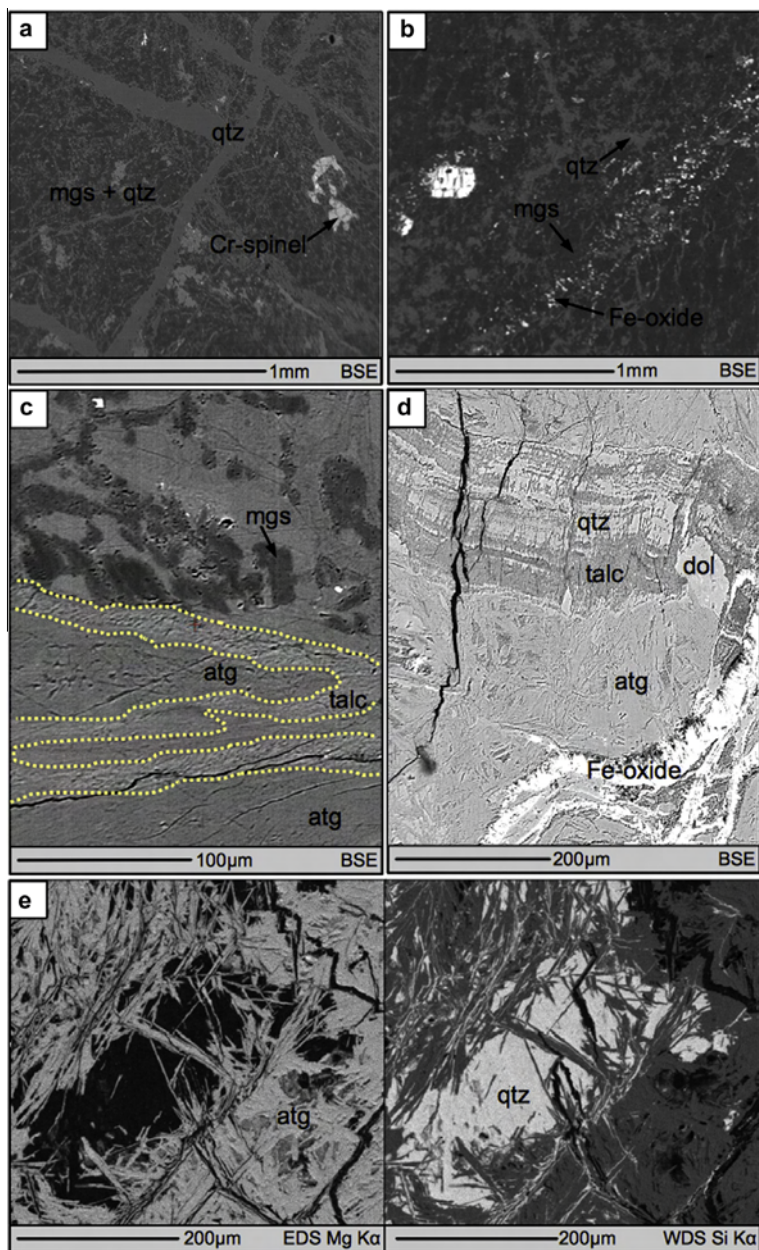


Fig. 5. Micro-textures in samples from transects across the listvenite–serpentinite transition of the main magnesite-quartz listvenite band at Wadi Mansah, back-scattered electron (BSE) images and elemental maps. (a) A representative BSE image of listvenite sample OM09-15 shows fine, intergrown magnesite (dark gray, “mgs”) and quartz cut by dense networks of quartz veins (medium gray, “qtz”). Fine-grained, Fe-oxides (white) are scattered through the matrix, and larger, relict Cr-spinels (very light gray) attest to the peridotite protolith. (b) BSE image of magnesite (dark gray) and quartz (light gray), lacking sharply defined monomineralic vein networks, and intergrown with abundant fine-grained Fe-oxide (white) in listvenite sample OM10-03. (c) Talc-antigorite vein adjacent to magnesite intergrown with antigorite in sample OM10-02 from the listvenite–serpentinite transition zone. Yellow dotted lines are added to emphasize the boundary between talc and antigorite. Although not pictured here, magnesite is also present within these small, mixed talc-antigorite veins. (d) Mixed veins of quartz, talc, and Fe-oxide and dolomite (“dol”) in antigorite (“atg”) in sample OM09-12 from the listvenite–serpentinite transition zone. (e) Bladed antigorite intergrown with quartz in sample OM09-12, shown in an WDS elemental map of Si content (left) and an EDS elemental map of Mg content (right). (For interpretation of the references to color in this figure legend, the reader is referred to the web version of this article.)

presented Fig. 8 and Supplementary Table S13. Measured $^{87}\text{Sr}/^{86}\text{Sr}$ values in the listvenite range from 0.7095 to 0.7135. Sr isotopic ratios probably remained largely unchanged over time due to low Rb content. Most of these

Sr isotopic ratios are significantly higher than in Cretaceous to modern seawater (Veizer et al., 1999), and are consistent with our new values within the underlying allochthonous metasediments, which range from 0.7061 to 0.7189

(corresponding to values of 0.7061–0.7122 at 96 Ma during emplacement of the ophiolite, (Hacker et al., 1996)). Even more radiogenic strontium isotope ratios have been reported in autochthonous clastic sediments, with $^{87}\text{Sr}/^{86}\text{Sr}$ values up to 0.772 (Weyhenmeyer, 2000).

The presence of K-bearing fuchsite in magnesite-quartz listvenite sample OM10-26 provides a host for Rb, allowing for differential in-growth of ^{87}Sr and construction of an internal isochron (Fig. 9, Supplementary Table S14). The data for this sample yield an isochron age of 97 ± 29 Ma, calculated using ISOPLOT, model 3 (Ludwig, 2003). The scatter in these data exceed the expected scatter due to analytical errors, suggesting “geologic” scatter may result from non-uniform initial strontium isotope ratios or later alteration resulting in addition or loss of Rb and/or Sr from some phases.¹

3.4. Stable isotopes

$\Delta 47$, $\delta^{13}\text{C}$, $\delta^{18}\text{O}$, and clumped isotope temperatures in carbonate from listvenite and underlying metasediments are reported in Table 2, and illustrated in Fig. 10. A table of all clumped isotope measurements, including known-temperature magnesite samples, standards, and heated gases, is presented in Supplementary Table S2. Clumped isotope temperatures derived from the quadratic fit to all Caltech-derived dolomite and synthetic calcite calibration data employed by Bristow et al. (2011) agreed better with the known temperatures of synthetic magnesite and low temperature playa magnesite than other empirical and theoretical calibrations (Ghosh et al., 2006; Guo et al., 2009; Dennis and Schrag, 2010; Dennis et al., 2011; Bristow et al., 2011), as presented in Supplementary Figure S4. The clumped isotope temperatures discussed here are derived using the calibration of Bristow et al. (2011), but results using other calibrations are presented in Supplementary Table S2 for comparison. Measured $\Delta 47$ values correspond to temperatures of 61–114 °C for listvenite, 37–71 °C for samples from the listvenite–serpentinite transition zones, and 64–171 °C for underlying metasediment.

$\delta^{13}\text{C}$ values in listvenite range from -2.5‰ to $+1.0\text{‰}$ PDB and overlap metasediment values (Fig. 10a and c). Carbonate $\delta^{18}\text{O}$ values range from -9.3‰ to -6.5‰ PDB in magnesite-quartz listvenite and -11.3‰ to -4.9‰ PDB in dolomite-quartz listvenite. In the allochthonous metasediments directly underlying the listvenite in Wadi Mansah, $\delta^{18}\text{O}$ values range from -10.0‰ to -8.9‰ PDB in calcite and are -9.4‰ PDB in dolomite. $\delta^{18}\text{O}$ values in quartz (Supplementary Table S5) range from 21.5‰ to 23.8‰ SMOW in magnesite-quartz listvenite and from 16.5‰ to 25.7‰ SMOW in dolomite-quartz listvenite and are correlated with $\delta^{18}\text{O}$ in carbonate (Fig. 11).

¹ The nominal analytical errors may underestimate the uncertainty of the entire procedure, given that two separate dissolutions of bulk powder of OM10-26 differ in $^{87}\text{Sr}/^{86}\text{Sr}$ by ~ 0.003 , more than two orders of magnitude higher than the standard deviation of filament duplicates prepared from the same dissolution/purification.

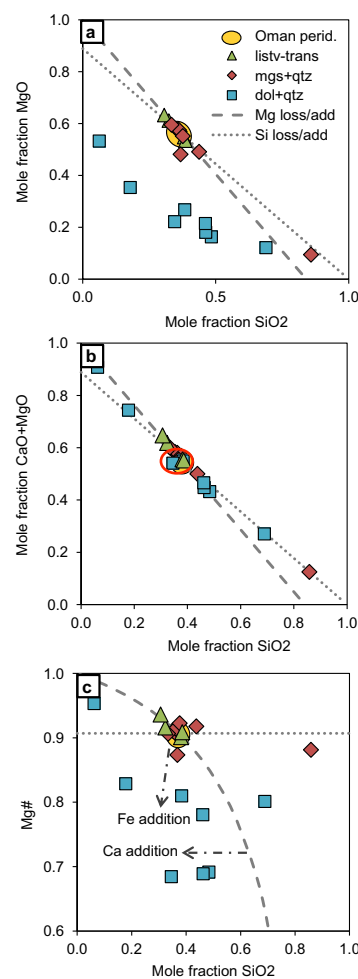


Fig. 6. (a) Volatile-free molar MgO versus molar SiO_2 . (b) Volatile-free molar $\text{MgO} + \text{CaO}$ versus molar SiO_2 . (c) Molar $\text{Mg}/(\text{Mg} + \text{Fe})$, or $\text{Mg}\#$, versus molar SiO_2 . Dashed and dotted gray lines show the expected composition of an average peridotite from the Samail ophiolite perturbed only by removal or addition of Mg or Si, respectively. Quartz + magnesite listvenites compositions (red diamonds) and rocks from the listvenite–serpentinite transition zone (green triangles) mostly fall within the range of typical, partially serpentinized peridotite composing the mantle section in the nearby portions of the ophiolite, as represented by the range of data reported by Godard et al. (2000) and Hanghøj et al. (2010) (yellow oval). Dolomite + quartz listvenite compositions (blue squares) span a broader range of Si concentrations and are deficient in Mg, primarily due to variable Ca addition. Low $\text{Mg}\#$'s in the dolomite + quartz listvenites could be explained by Mg removal accompanied by Ca addition, and/or by Fe addition. (For interpretation of the references to color in this figure legend, the reader is referred to the web version of this article.)

4. DISCUSSION

4.1. Timing of listvenite formation

The 97 ± 29 Ma Rb–Sr age derived from magnesite-quartz listvenite sample OM10–26 suggests that listvenite formation occurred during emplacement of the ophiolite, which was initiated ~ 96 Ma and continued until ~ 78 Ma

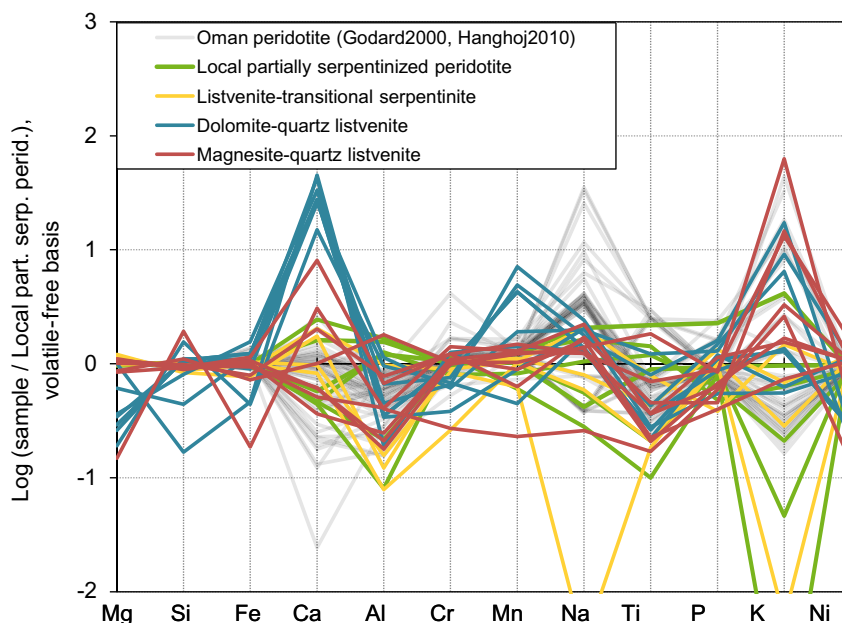


Fig. 7. XRF data from listvenites and associated rocks compared to the composition of fresh harzburgites and dunites from the Samail ophiolite (Godard et al., 2000; Hanghøj et al., 2010). XRF data are projected from loss-on-ignition (LOI), and the volatile-free composition is ratioed to the average composition of partially serpentinized peridotite from Wadi Mansah. The logarithm of these ratios are plotted here, such that a value of zero is identical in composition to that of average partially serpentinized peridotite, positive values indicate enrichments relative to the protolith, and negative values indicate depletions relative to the protolith. Magnesite + quartz listvenite (red), dolomite + quartz listvenite (blue), and samples listvenite–serpentine transition zone (yellow) are similar in composition to partially serpentinized peridotite (green) and fresher harzburgites and dunites from the Samail ophiolite (gray), aside from variable enrichments in Ca, K, and Mn. Most listvenite samples have some enrichment in K (although K is also variable in the protolith). Dolomite + quartz listvenite samples are highly enriched in Ca and moderately enriched in Mn. (For interpretation of the references to color in this figure legend, the reader is referred to the web version of this article.)

(e.g., Hacker et al., 1996; Rioux et al., 2013), rather than during a period of increased heat flow in the early Tertiary (~36–40 Ma) as proposed by Wilde et al. (2002). This age is also consistent with mapping of late Paleocene to Eocene conglomerates unconformably overlying the listvenite (Villey et al., 1986). Although previous workers have hypothesized that listvenite formation in Oman occurred subsequent to obduction, syn-obduction metasomatism has been proposed to explain other listvenite occurrences in ophiolites worldwide (e.g., Buisson and Leblanc, 1987; Plissart et al., 2009).

4.2. Protolith

Listvenite formed from partially serpentinized harzburgites and dunites at and near the base of the mantle section of the Samail ophiolite. Many samples of magnesite-quartz listvenite overlap entirely the bulk compositions of adjacent partially serpentinized peridotite and of peridotite elsewhere in the ophiolite (Godard et al., 2000; Hanghøj et al., 2010), as shown in Fig. 6 and 7. In partially serpentinized peridotite enclosing the listvenite at Wadi Mansah, the degree of serpentinization varies from 30% to 100%, with relict olivine becoming more abundant with increasing distance from contacts the listvenite. Approximately 30–60% serpentinization likely occurred during initial suboceanic alteration (Boudier et al., 2010) prior to listvenite formation. Whereas early serpentinization formed

mesh-texture lizardite and chrysotile, during subsequent carbonation, antigorite formed in the listvenite–serpentine transition zones, perhaps stabilized by elevated silica activity in the fluid associated with listvenite formation. In serpentinized peridotite just beyond these transition zones, the high degree of serpentinization suggests that the fluid pathways that allowed for listvenite formation have also facilitated additional hydration of peridotite. In some of our partially-serpentinized peridotite samples, more Fe-rich lizardite (e.g., Mg# ~85) rims or replaces relict olivine in the mesh cores, accounting for ~10% of the serpentine present (Supplementary Figure S3 and related text in Supplementary Section S.1). These limited amounts of low-Mg# serpentine likely represent later, lower-temperature alteration (Streit et al., 2012), superimposed on pre- and syn-obduction serpentinization.

This suggests that 20–90% relict olivine may have been available in the protolith prior to listvenite formation. Combined with the observation that many magnesite listvenites have compositions equivalent to mantle harzburgites from the Samail ophiolite + CO₂, with little or no dissolution and removal of other chemical components (Section 3.2), these data imply very large volume changes during listvenite formation. For example, the volume increase for the reaction forsterite + 2 CO₂ = 2 magnesite + quartz, computed as the difference between product volume – reactant volume divided by the reactant volume, is approximately 80%.

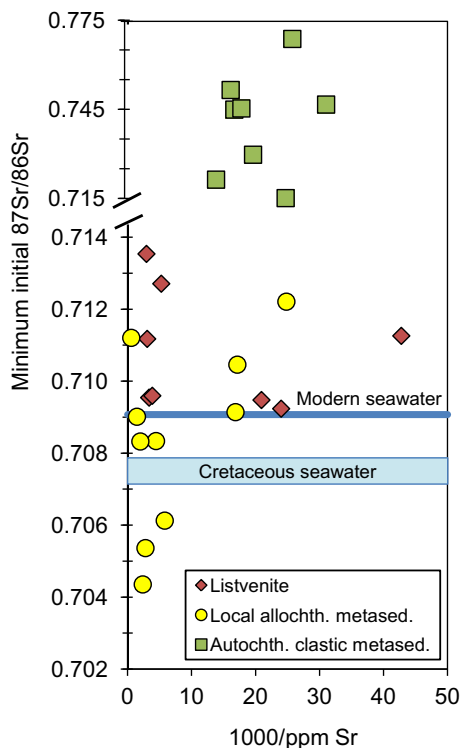


Fig. 8. Minimum initial Sr isotope ratios for listvenites (red diamonds), local underlying allochthonous metasediments and metavolcanics (yellow circles), and autochthonous clastic metasediments from Weyhenmeyer (2000) (green squares), compared to Sr isotope ratios in modern and Cretaceous seawater (Veizer et al., 1999). Age-corrected Sr isotope ratios were calculated assuming an age of 96 Ma. For the listvenite and local allochthonous metasediments analyzed for this study, the age corrected ratios were calculated using measured $^{87}\text{Sr}/^{86}\text{Sr}$ and Rb:Sr ratios. Rb concentrations were not reported for the autochthonous clastic metasediments from Weyhenmeyer (2000), so an estimated upper bound Rb concentration of 2000 ppm was used with the measured $^{87}\text{Sr}/^{86}\text{Sr}$ and Sr concentration, to estimate a minimum Sr isotope ratio at 96 Ma for these samples. (For interpretation of the references to color in this figure legend, the reader is referred to the web version of this article.)

4.3. Temperature constraints

We derive temperature constraints for the formation of listvenite from mineral parageneses (80–130 °C) and clumped isotopes (average = 90 °C), consistent with oxygen isotopes in carbonate and quartz for fluid $\delta^{18}\text{O}$ values near 0‰ SMOW. Most of the temperatures recorded by our listvenite samples are warmer than the inferred maximum temperatures of ~65 °C for listvenite formation proposed by Wilde et al. (2002), and significantly cooler than temperature estimates for other listvenite bodies worldwide: about 210–280 °C in Canada (Andrew, 1985; Madu et al., 1990; Schandl and Wicks, 1993; Schandl and Gorton, 2012), 280–340 °C in Armenia (Spiridonov, 1991), 200–300 °C in eastern Australia (Oskierski et al., 2013), 250–350 °C in California (Weir and Kerrick, 1987), and 150–250 °C in Morocco (Buisson and Leblanc, 1987).

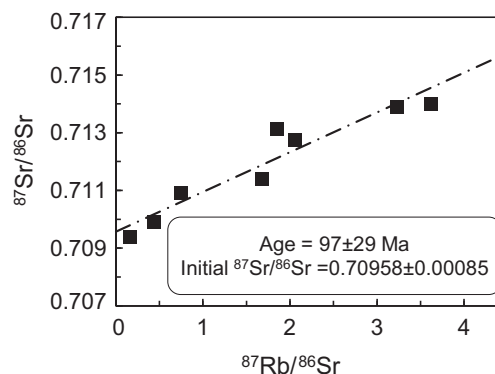


Fig. 9. An internal Rb–Sr isochron constructed from different fractions of varying magnetic susceptibility from magnesite–quartz listvenite OM10-26 yields an age of 97 ± 29 Ma, consistent with the timing of emplacement of the Samail ophiolite. Age calculated using ISOPLOT model 3 (Ludwig, 2003).

4.3.1. Temperatures from mineral parageneses

The similarity of the volatile-free bulk compositions of magnesite–quartz listvenites to those of relatively unaltered Oman harzburgites suggests a relatively simple alteration history, allowing us to make inferences about the conditions of peridotite carbonation. Temperature– X_{CO_2} phase diagrams (where X_{CO_2} indicates mole fraction $\text{CO}_2/(\text{H}_2\text{O} + \text{CO}_2)$) for the $\text{MgO}–\text{SiO}_2–\text{H}_2\text{O}–\text{CO}_2$ system (e.g., Fig. 12) were calculated at pressures of 1 MPa to 10 GPa using THERMOCALC (Holland and Powell, 1998, 2011) to examine the regions of stability for the assemblages observed in listvenite (magnesite + quartz) and in the listvenite–serpentinite transition zones (magnesite + talc + antigorite, quartz + talc + antigorite, quartz + antigorite). Using THERMOCALC, the reaction antigorite + 30 quartz = 16 talc + 15 H_2O is calculated to occur at temperatures of $\sim 80 \pm 3$ °C for pressures between 1 MPa and 1 GPa. As for the reaction chrysotile + 2 quartz = talc + H_2O (Streit et al., 2012), the calculated temperature of the reaction antigorite + 30 quartz = 16 talc + 15 H_2O reaction is higher ($\sim 130 \pm 15$ °C) if the thermodynamic database of Gottschalk (1997) is used rather than that of Holland and Powell (2011). The primary effect of increasing pressure is to shift phase boundaries involving magnesite to lower X_{CO_2} (e.g., Fig. 13).

The occurrence antigorite + quartz + talc in the listvenite–serpentinite transition zones (e.g., Fig. 5d and e) thus provides a temperature estimate of 80–130 °C for the margin of the listvenite bands. This also provides constraints for the temperature of listvenite formation, as it is unlikely that a strong thermal gradient was maintained across the <2 m wide transition zone between listvenite and partially serpentinized peridotite. The change in parageneses, from magnesite + quartz to antigorite + quartz (\pm talc, \pm carbonate minerals) can be understood in terms of a decrease in X_{CO_2} in the fluid across the listvenite boundary. Near the temperature of the invariant point, the range of CO_2 concentrations over which talc + magnesite is stable without serpentine is very small, so if temperature and X_{CO_2} were restricted to a relatively small range near the invariant point

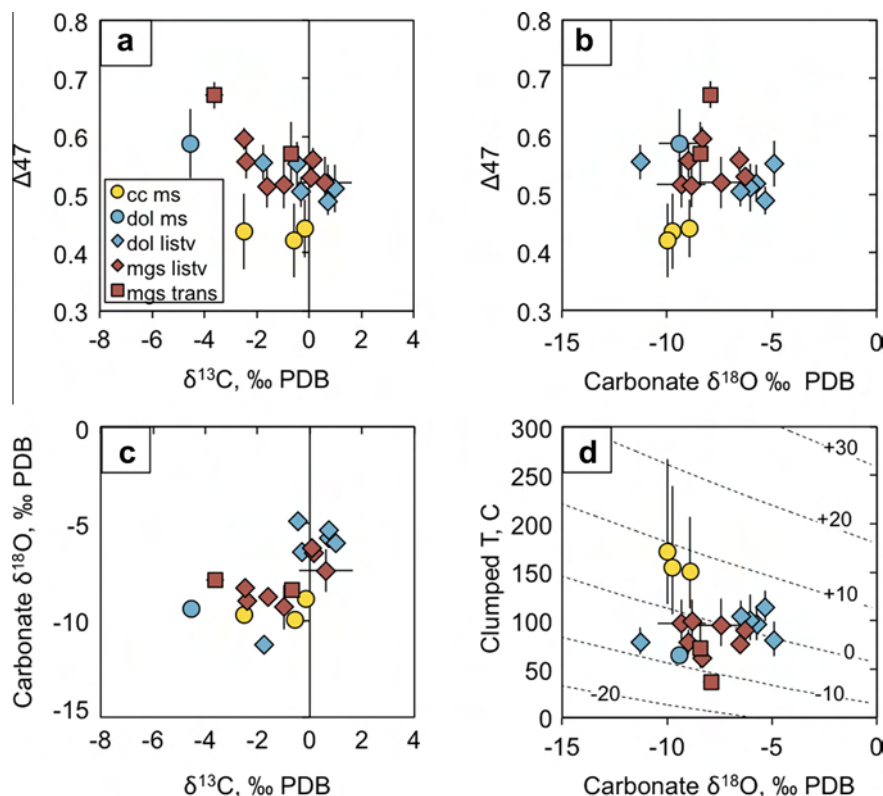


Fig. 10. Cross-plots of $\Delta 47$, $\delta^{13}\text{C}$, $\delta^{18}\text{O}$, and clumped isotope temperature (calculated using calibration of [Bristow et al. \(2011\)](#)) in listvenite and associated lithologies: magnesite + quartz listvenite (red diamonds), dolomite + quartz listvenite (blue diamonds), calcite-bearing metasediment (yellow circles), dolomite-bearing metasediment (blue circle). In part (d), dashed lines indicate the temperature- $\delta^{18}\text{O}$ relationship for magnesite, as calculated by [Schauble et al. \(2006\)](#) for constant fluid $\delta^{18}\text{O}$ ranging from -10‰ to $+30\text{‰}$ SMOW, as indicated along curves. The slopes of corresponding curves for calcite and dolomite (not plotted) are similar to those for magnesite (e.g., [Kim and O'Neil, 1997](#); [Vasconcelos et al., 2005](#)). $\delta^{13}\text{C}$ values cluster within -3‰ to $+1\text{‰}$, with overlapping values for listvenites and metasediments. Carbonate $\delta^{18}\text{O}$ values in listvenite mostly fall within a range of -5‰ to -10‰ PDB. If all listvenite samples formed from fluids of similar isotopic composition, these $\delta^{18}\text{O}$ values imply a much narrower range of temperatures than the $37\text{--}114\text{ °C}$ recorded by clumped isotopes, e.g., $\sim 90\text{--}110\text{ °C}$ for $\delta^{18}\text{O}_{\text{fluid}} = 0\text{‰}$ SMOW and $\delta^{18}\text{O}_{\text{magnesite}}$ between -6‰ and -10‰ PDB. (For interpretation of the references to color in this figure legend, the reader is referred to the web version of this article.)

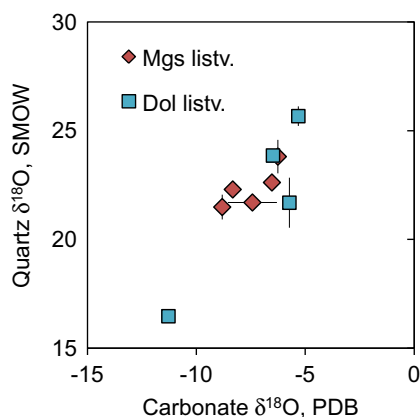


Fig. 11. $\delta^{18}\text{O}$ values in quartz are correlated with $\delta^{18}\text{O}$ in carbonate (red diamonds = magnesite + quartz listvenite, blue squares = dolomite + quartz listvenite). (For interpretation of the references to color in this figure legend, the reader is referred to the web version of this article.)

during alteration, this could explain why talc is not observed without coexisting serpentine in association with the listvenite bodies at Wadi Mansah.

4.3.2. Temperatures from clumped isotope thermometry and oxygen isotopes

Average clumped isotope temperatures in listvenite ($90 \pm 15\text{ °C}$) agree well with the petrological temperature estimates of $80\text{--}130\text{ °C}$ for the antigorite + 30 quartz = 16 talc + 15 H_2O reaction. These temperatures are significantly lower than clumped isotope temperatures recorded by calcite-bearing metasediments within $\sim 100\text{ m}$ of the basal thrust beneath the listvenite ($\sim 160\text{ °C}$). These metasediments are mapped as part of the metamorphic sole, some of which experienced peak temperatures as high as 800 °C in the early stages of emplacement of the ophiolite ([Ghent and Stout, 1981](#)). The clumped isotope temperatures in the calcite-bearing metasediments may represent closure temperatures, as clumped isotope closure temperatures range from ~ 150 to 250 °C in marbles and carbonates ([Dennis and Schrag, 2010](#)).

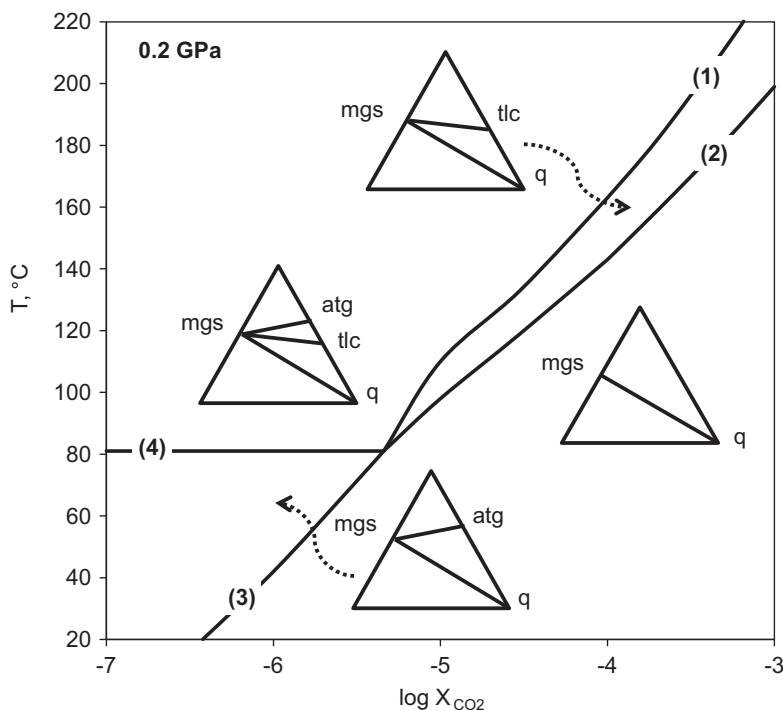


Fig. 12. Temperature- X_{CO_2} diagram depicting phase equilibria in the MgO-SiO₂-H₂O-CO₂ system from 20 °C to 220 °C at 0.2 GPa. X_{CO_2} = molar CO₂/(CO₂ + H₂O). Boundaries represent reactions between magnesite (mgs), antigorite (atg), talc (tlc), and quartz (q), calculated using THERMOCALC (Holland and Powell, 1998, 2011). Reactions: (1) $2\text{atg} + 45\text{CO}_2 = 45\text{mag} + 17\text{tlc} + 45\text{H}_2\text{O}$, (2) $3\text{mag} + 4\text{q} + \text{H}_2\text{O} = \text{tlc} + 3\text{CO}_2$, (3) $48\text{mag} + 34\text{q} + 31\text{H}_2\text{O} = \text{atg} + 48\text{CO}_2$, (4) $\text{atg} + 30\text{q} = 16\text{tlc} + 15\text{H}_2\text{O}$.

Although clumped isotope temperatures in listvenite are broadly in agreement with petrological temperature estimates, the broad range of $\Delta 47$ values from listvenite samples, compared with the narrower range of $\delta^{18}\text{O}$ values in both carbonate and quartz, suggests that some $\Delta 47$ values may have been subject to bond re-ordering after the initial precipitation of the carbonate, or that carbonates in our samples are polygenetic, recording several episodes of formation or recrystallization. For example, the relative standard deviation of clumped isotope temperatures in magnesite listvenites is 16%, while the relative standard deviation of temperatures derived from conventional carbonate-water oxygen isotope thermometry in those same samples is only 7% (average temperature 110 ± 7 °C) calculated using magnesite-water oxygen isotope fractionation factors from Chacko and Deines (2008) and an assumed fluid $\delta^{18}\text{O}$ of 0‰ SMOW (Supplementary Table S6).

The clumped isotope signal could have been modified by multiple episodes of formation and/or recrystallization of carbonates in our samples, over a range of temperatures. For example, minor late precipitation of carbonates and/or recrystallization could have occurred during low temperature, post-emplacment interaction with groundwater. Mixing of CO₂ derived from this younger, low temperature component with CO₂ derived from carbonate precipitated during listvenite formation could lead to anomalous $\Delta 47$ values. Mixing of CO₂ from carbonates with different $\delta^{13}\text{C}$ and/or $\delta^{18}\text{O}$ may result in a $\Delta 47$ value of the mixture that is not only non-linear with respect to the weighted

proportions of the endmembers, but that is outside the range of $\Delta 47$ values of the two endmembers (Eiler and Schauble, 2004). The highest $\Delta 47$ values we observe in listvenite correspond to the lowest $\delta^{13}\text{C}$ values, so it is possible that these high $\Delta 47$ values are artificially high as the result of non-linear mixing with a carbonate precipitated from a source with low $\delta^{13}\text{C}$, such as meteoric water for example.

Regardless of mechanisms that may have generated higher $\Delta 47$ values in some samples, all but two of the clumped isotope temperatures in listvenite and the listvenite-serpentine transition zones fall between 70 and 115 °C, similar to temperatures estimated from mineral parageneses in the transition zones.

Carbonate-quartz oxygen isotope fractionations cannot provide reliable temperature estimates in our listvenite samples, due in part to a lack of temperature sensitivity and uncertainty in the fractionation factors for magnesite and dolomite. However, carbonate and quartz appear to be isotopic equilibrium in most samples (at least for some choices of fractionation factors), and temperatures derived from oxygen isotope fractionation between water with assumed $\delta^{18}\text{O}$ values near 0‰ SMOW and magnesite, dolomite, or quartz from listvenite generally overlap with those derived from mineral parageneses and clumped isotope thermometry (see Supplementary Table S6). Additional discussion of carbonate and quartz $\delta^{18}\text{O}$ and related tables and figures can be found in the Electronic Supplement (Supplementary Tables S5 and S6, Supplementary Figure S8, and related text in Supplementary Section S.4).

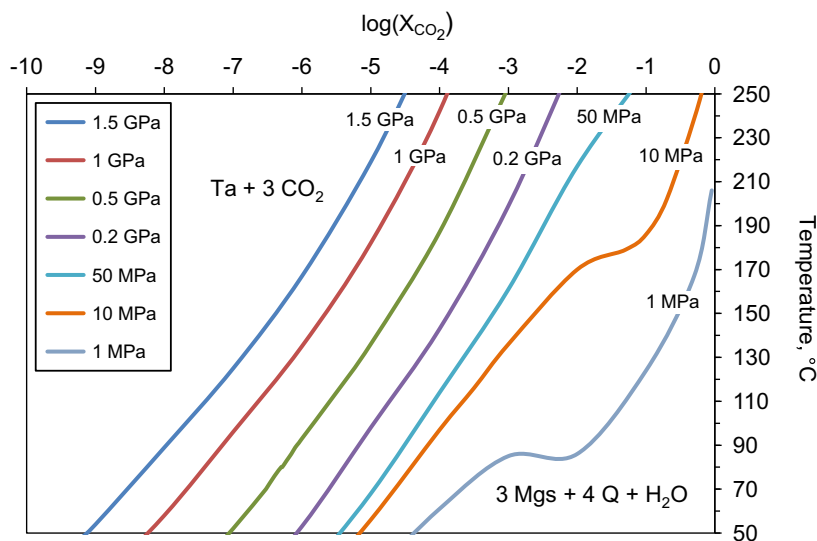


Fig. 13. T - X_{CO_2} phase boundaries for the reaction $3 \text{ magnesite} + 4 \text{ quartz} + \text{H}_2\text{O} = \text{talc} + 3 \text{ CO}_2$, calculated in THERMOCALC (Holland and Powell, 1998, 2011) for pressures from 1 MPa to 1.5 GPa.

4.4. Fluid sources for listvenite formation

Sr isotope values can be viewed as a tracer for Sr from the source of the CO_2 -bearing fluids that formed listvenites, and by association, for Ca and other elements that were also enriched during formation of listvenites. In Quaternary low-temperature carbonate veins in serpentinite and travertine from the Samail ophiolite, $^{87}\text{Sr}/^{86}\text{Sr}$ is higher than mantle values but less than or equal to modern seawater values, suggesting that Sr in those rocks was derived from a combination of (a) seawater, meteoric water, or ground water in Oman with $^{87}\text{Sr}/^{86}\text{Sr} \leq 0.709$ (Weyhenmeyer, 2000) and (b) mantle Sr with $^{87}\text{Sr}/^{86}\text{Sr}$ extending down to 0.703 (Gerbert-Gaillard, 2002; see data compilation in Kelemen et al., 2011, Supplementary Figure 3 and associated text). By contrast, the age corrected Sr isotopic ratios of listvenites (0.7092–0.7135 $^{87}\text{Sr}/^{86}\text{Sr}$ at 96 Ma) must include substantial Sr from sources that had $^{87}\text{Sr}/^{86}\text{Sr}$ higher than seawater. Our samples of allochthonous metasediments directly underlying the listvenite at the Wadi Mansah locality include several suitably radiogenic sources ($^{87}\text{Sr}/^{86}\text{Sr}$ up to 0.7122 at 96 Ma). Sr may also have been derived from underlying autochthonous sediments, which include even more radiogenic clastic sediments with $^{87}\text{Sr}/^{86}\text{Sr} \sim 0.72$ –0.77 at 96 Ma (Weyhenmeyer, 2000). (See Fig. 8.) Carbonate $\delta^{13}\text{C}$ from listvenites and metasediments from Wadi Mansah also overlap, with most values between 2.5‰ and +1‰ PDB, supporting a sediment-derived source of carbon in the listvenite (Fig. 10a and c).

The fluid mediating Sr, CO_2 , Ca, and K transfer could have been derived from sediment-equilibrated seawater released upon compaction of pore space, or from devolatilization of hydrous minerals in sediments. This would also be consistent with stable isotope data. Assuming the temperatures indicated by mineral paragenesis and the highest recorded clumped isotope temperatures

are most representative of the temperature of listvenite formation, $\delta^{18}\text{O}$ compositions of carbonate and quartz in listvenite would be in equilibrium with average fluid $\delta^{18}\text{O}$ values ranging from about $-1 \pm 3\text{‰}$ at 80 °C to $5 \pm 3\text{‰}$ at 130 °C. The variability in these fluid $\delta^{18}\text{O}$ values averaged over all samples and choices of fractionation factors is due to both variability between samples and variability between available fractionation factors (See Supplementary Figure S8 and related text in Supplementary Section S.4 for additional details on $\delta^{18}\text{O}$ in listvenites.). The $\delta^{18}\text{O}$ of Cretaceous seawater in sedimentary pore space would evolve to about 5–8‰ if it were fully equilibrated with authigenic calcite and to about –8‰ to –5‰ if it were fully equilibrated with clastic quartz.² Thus, the listvenite $\delta^{18}\text{O}$ values are within the range expected for fluid derived from subducting sediments.

The formation of listvenite during the emplacement of the Samail ophiolite provides a window into CO_2 metasomatism in the shallow hanging wall of subduction zones. Along typical subduction zone geotherms, slab-top temperatures around 80–130 °C are reached at depths of ~10–50 km (e.g., Rüpke et al., 2004; Syracuse et al., 2010). Listvenite a few hundred meters above the basal thrust would experience higher temperatures, making these maximum depth estimates for the formation of the listvenite. Thus, it is likely that listvenite formation occurred at pressures of roughly 0.2–1.5 GPa. Geological data also provide constraints on pressure. The crustal section of the Samail ophiolite, overlying mantle peridotites, is 5–7 km thick (Nicolas et al., 2000). The mantle section of the

² assuming an initial temperature of 10 °C; initial $\delta^{18}\text{O}$ of –1‰ for seawater, 31‰ for calcite, 6‰ for quartz; initial porosity of 0.70; final temperature of 80–130 °C; final porosity of 0.5; and mineral–water fractionation factors from Friedman and O’Neil (1977).

ophiolite, overlying the basal thrust, had a variable thickness and is up to 15 km thick in present day sections (e.g., Boudier and Coleman, 1981). This yields a combined thickness of 5–22 km (0.1–0.7 GPa) for the section overlying the Wadi Mansah listvenites at the time of their formation.

At pressures between 0.2 and 1.5 GPa, high concentrations of CO₂ in the fluid are not required to stabilize magnesite-quartz listvenites (Fig. 13). The minimum mole fraction of CO₂ necessary to stabilize magnesite + quartz at temperatures of 80–130 °C varies from $X_{\text{CO}_2} \sim 10^{-8}$ – 10^{-7} at 1.5 GPa to $X_{\text{CO}_2} \sim 10^{-5}$ – 10^{-4} at 0.2 GPa. If listvenite formation occurred during emplacement of the ophiolite and the antigorite-quartz-talc assemblage observed at the margins of the listvenite body is indicative of peak temperatures, then Cretaceous seawater CO₂ concentrations, equivalent to $X_{\text{CO}_2} \sim 10^{-4}$ (Wallmann, 2001), would be sufficient to stabilize magnesite + quartz. In contrast, formation of listvenite via low pressure alteration involving shallow groundwater, as suggested by Stanger (1985) and Wilde et al. (2002), would require a more CO₂-rich fluid (e.g., $X_{\text{CO}_2} \sim 10^{-2}$ at 1 MPa) at similar temperatures. It should be noted that the approach to thermodynamic modeling and choice of thermodynamic databases can have a significant effect on the calculated CO₂ concentrations required to stabilize the magnesite + quartz assemblage. For example, Klein and Garrido (2011) investigated phase equilibria in the MgO–SiO₂–H₂O–CO₂ system through reaction path models of reaction between serpentinite or dunite and CO₂-enriched seawater at 50 MPa, using the software packages SUPCRT92 (Johnson et al., 1992) and EQ3/6 (Wolery, 1992). In their models, the boundary between magnesite + quartz and talc + quartz at 100 °C occurred at a CO₂ activity of $10^{-2.5}$, whereas our THERMOCALC calculations (Fig. 13) place this boundary at X_{CO_2} of $10^{-4.3}$ at 100 °C and 50 MPa.

Metamorphic decarbonation of sediments is not expected to occur beneath the forearc in subduction zones (e.g., Kerrick and Connolly, 2001; Gorman et al., 2006). However, carbonate dissolution from metasediments in aqueous fluids has been shown to be a source of CO₂ for metasomatic processes in subduction zones (e.g., Sakai et al., 1990; Haggerty, 1991; Mottl et al., 2004; Konno et al., 2006; Lupton et al., 2006; Frezzotti et al., 2011). Carbonate dissolution and release of CO₂-enriched fluids could occur gradually as pore-water in equilibrium with sediments is released during compaction, or more suddenly as fresh water is released via dehydration of minerals in the sediments and reacts with carbonate-bearing sediments, for example during the smectite to illite transition at ~ 75–150 °C (Lynch, 1997). The resulting fluid, saturated in the minerals in the sedimentary host rock, would rise into the overlying mantle, perhaps migrating first along the top of the subducting plate or along faults subparallel to the top of the plate. Focusing of fluid flow could yield localized, high fluid fluxes. Seafloor fluid expulsion in forearcs demonstrates that water released by dehydration of subducted sediments is transported both vertically and trench-ward by deep-seated thrust faults (Hensen et al., 2004). In Oman, listvenite follows major fault zones, and the antiformal

structure of the Wadi Mansah locality, if present during carbonation, could also have localized fluid flow.

Rough mass balance calculations show that the flux of CO₂-bearing fluid from the subducted sediments would be sufficient for the formation of the extensive listvenites observed in Oman. A 100-meter thick column of listvenite containing 30 wt% CO₂ contains $\sim 2.5 \times 10^4$ kg C/m². If we assume the carbon concentration in the pore fluid was ~100 ppm (Cretaceous seawater (Wallmann, 2001)), then the mass of sediment-derived fluid reacted to form this listvenite would be at least $\sim 2.5 \times 10^8$ kg/m², or ~12 kg/year/m² if averaged over ~20 Ma of obduction (Hacker et al., 1996).

In the case of pore water release, sediments start with a pore volume fraction of ~0.4–0.7, and after rapid compaction to ~0.2 porosity in the first few kilometers of burial (or subduction), porosity decreases by ~0.04/km, yielding ~1.4 wt% water/km (Bond and Kominz, 1984). Thus, for a hypothetical 2–3 km column of sediment (e.g., thickness of the Hawasina sediments underlying the Samail ophiolite) being subducted at a rate of 6 cm/year, ~3–5 kg of pore water/m²/year would be expelled by compaction beneath the overlying mantle. Thus sufficient fluid for observed listvenite thicknesses could be derived from seawater expelled from compacted sediments, particularly if fluids were channeled from a source area 2–4 times the area of the listvenite or if fluids were further enriched in CO₂ during subduction, as calcite solubility should increase with depth (e.g., Dolejs and Manning, 2010; Coto et al., 2012; Kelemen and Manning, 2015).

Mineral dehydration could also contribute CO₂-bearing fluid. Average global subducting sediment (GLOSS) (Plank and Langmuir, 1998) contains ~7% mineral-bound water, whereas clay-rich, fine-grained clastic sediments contain even more. Release of this water and dissolution of carbonates in sediment could provide an additional source of carbon-bearing fluid for listvenite formation.

Considerable amounts of water can be released by mineral transformations that involve partial dehydration, such as the transformation of clay minerals to micas and chlorite. For example, between 75 and 150 °C, the transition of smectite to illite releases ~30 wt% H₂O in mudstones and shales (Lynch, 1997). For a 2–3 km thick sediment section including 50% clay-rich lithologies, subducting at 6 cm/year, this would produce ~2 kg of water/m²/year. Transformations of hydrated minerals, including expulsion of interlayer water and conversion of opal-A to opal-CT at 30–80 °C and expulsion of interlayer water and conversion of smectite to illite at 50–150 °C, have previously been proposed as the source of low-chlorinity waters upwelling at serpentine mud volcanoes in the Mariana forearc (Mottl et al., 2004) and at seafloor sites in accretionary prisms (Bebout, 2013).

Additional mineral dehydration and decarbonation are predicted to occur at greater depths in forearc environments (e.g., Rüpke et al., 2004; Gorman et al., 2006). Modeling by Rüpke et al. (2004) indicates that ~50% of the mineral-bound water in sediments should be released by dehydration in a pulse between 30 and 40 km depth. A 3 km column of sediment being subducted at a rate of 6 cm/year would

be expected to release $\sim 8\text{--}13 \times 10^3$ kg $\text{H}_2\text{O}/\text{m}/\text{year}$ in this dehydration front. Gorman et al. (2006) predict a pulse of dehydration and decarbonation at $\sim 70\text{--}90$ km depth, resulting in a fore arc CO_2 flux of $11\text{--}37$ kg $\text{CO}_2/\text{m}/\text{year}$ for a 500 m sediment section. If some of these fluids migrated up the subduction zone and then reacted with peridotite at shallower depth, this could also play a role in the formation of listvenite.

In summary, there are at least three viable fluid sources for listvenite formation during emplacement of the Samail ophiolite and in the shallow hanging wall of subduction zones worldwide: (1) compaction of pore waters from footwall metasediments, (2) low temperature dehydration of opal and clay minerals in footwall metasediments, and (3) higher temperature metamorphic devolatilization reactions coupled with fluid migration up the subduction zone.

4.5. Implications for carbon capture and storage (CCS)

Carbonation of peridotite has been proposed as a method for permanent CO_2 storage (e.g., Seifritz, 1990; Lackner et al., 1995) as well as distributed, geological capture of CO_2 (Kelemen and Matter, 2008; Kelemen et al., 2011). Natural analogs to *in situ* mineral carbon sequestration in ultramafic bodies present potential alternatives to *ex situ* mineral carbonation, avoiding the costs of mining, transporting, and treating ultramafic material (e.g., Cipolli et al., 2004; Hansen et al., 2005; Kelemen and Matter, 2008; Kelemen et al., 2011; Beinlich et al., 2012). However, a major concern regarding *in situ* carbonation is that the solid volume increases expected during peridotite carbonation could result in loss of porosity and permeability and armoring of reactive mineral surfaces, thereby limiting reaction progress (e.g., Xu et al., 2004; Hansen et al., 2005).

The presence of listvenite bodies demonstrates that geological carbonation of peridotite can progress to completion under natural conditions. Hansen et al. (2005) and Beinlich et al. (2012) suggest that the smaller solid volume increases associated with carbonation of serpentine rather than olivine reduce the chance of pore space clogging. In Oman, Stanger (1985) proposes that total serpentinization of the basal peridotite preceded formation of the “Amqat” lithology (listvenite). However, we find tens of percent of relict olivine in partially serpentinized peridotite sampled within meters of magnesite-quartz listvenites, as is common in peridotite throughout the mantle section of the ophiolite. These olivine relicts are frequently surrounded by high-Fe serpentine that likely formed later than listvenites, at lower temperatures (Streit et al., 2012), indicating that relict olivine was even more abundant during listvenite formation. In spite of the larger volume increases associated with carbonation of olivine, complete carbonation was attained within the listvenite zones.

This solid volume increase may even contribute to reaction progress by maintaining permeability through reaction-driven cracking (e.g., MacDonald and Fyfe, 1985; Jamtveit et al., 2008, 2009; Rudge et al., 2010; Kelemen et al., 2011; Kelemen and Hirth, 2012; Plümper et al., 2012). Although listvenite bodies in Oman probably follow pre-existing fault zones, and fluid flow may have been

localized along such faults, vein orientations in most of our listvenite samples are random or mutually orthogonal, and thus do not appear to be tectonically controlled. Quartz and carbonate veins occur as hierarchical networks extending down to micron scales, forming perpendicular vein sets suggestive of isotropic stresses (e.g., Figs. 3b and 5a). Reaction-driven cracking will be favored when reaction rates are high so that stress increases due to volume changes during reaction outpace viscous relaxation. At the inferred conditions of listvenite formation in Oman, $\sim 80\text{--}130$ °C and P_{CO_2} on the order of $\sim 1\text{--}5$ bars (seawater CO_2 concentrations at 0.2–1 GPa pressure), the fit of Kelemen and Matter (2008) to experimental data on olivine carbonation (O'Connor et al., 2005; Chizmeshya et al., 2007) yields rates $\sim 10^4\text{--}10^5$ higher than the carbonation rate at conditions of surficial weathering. These higher reaction rates may have promoted self-fracturing during peridotite carbonation.

5. CONCLUSIONS

Mineralogical and isotopic data support the hypothesis that listvenites in Oman formed during obduction of the Samail ophiolite, as CO_2 -enriched fluids derived from underlying sediments metasomatized hanging wall peridotite. An internal Rb–Sr isochron from one fuchsite-bearing listvenite sample yields an age of 97 ± 29 Ma, consistent with the timing of emplacement of the ophiolite, and with geologic mapping indicating that Late Cretaceous sediments unconformably overlie listvenite. Unlike carbonates formed via ongoing low-temperature alteration of peridotite, age-corrected listvenite Sr isotopic ratios are more radiogenic than seawater, suggesting input of radiogenic Sr from underlying metasediments. Mineral parageneses and carbonate clumped isotope thermometry suggest that listvenite formed at temperatures of $80\text{--}130$ °C. Along a subduction zone geotherm, these temperatures would be reached at $\sim 10\text{--}50$ km depth, where fluids could be released from subducted sediments either by compaction or partial dehydration reactions. At these pressures, the CO_2 concentration necessary to stabilize the magnesite + quartz assemblage is only slightly higher than seawater CO_2 concentrations. Equilibration of released water with carbonate in subducted sediments can yield fluids with sufficiently high CO_2 concentrations to form magnesite-quartz listvenite upon reaction with hanging wall peridotite, and the mass of fluid produced by compaction and partial dehydration reactions is sufficient to account for the observed mass of listvenite. These calculations are applicable to subduction zones worldwide. Globally, extensive carbonation of mantle wedge peridotite may be more common above subduction zones at the “leading edge of the mantle wedge” than has been previously recognized.

As a natural analog for carbon capture and storage via *in situ* mineral carbonation, listvenite formed in this kind of environment is promising. For example, schemes that involve enhanced convection of seawater through peridotite, rather than injection of high- P_{CO_2} fluids (Kelemen and Matter, 2008; Kelemen et al., 2011) may be expected to achieve complete carbonation of peridotite over time.

Even without extremely high CO₂ concentrations, and at temperatures below those corresponding to peak reaction rates in olivine carbonation experiments, complete carbonation of peridotite is attained in nature.

ACKNOWLEDGMENTS

This work would not have been possible without the support and generosity of many others. We thank everyone at the Geological Survey of Oman and the Directorate General of Minerals in the Ministry of Commerce and Industry, Sultanate of Oman, particularly H. Al-Azri, A. Al-Rajhi, and S. Al-Busaidi, for facilitating our fieldwork in Oman and S. Nasir of Sultan Qaboos University for providing us with an introduction to several listvenite localities in Oman. J. Eiler, S. Goldstein, Z. Wang, J. Gross, and C. Mandeville, along with N. Kitchen, K. Bergmann, A. Tripathi, J. Jweda, W. Jacobson, R. Lupien, M. Cai, T. Winger, B. Parks, J. Boesenberg, B. Goldoff and K. Benedetto are thanked for mentorship in and assistance with laboratory work. Many thanks are owed to G. Dipple and I. Power, E. Oelkers and Q. Gautier, M. Mazzotti and M. Werner, J. Ferry, and J.C. Deelman, who graciously shared their magnesite samples for assessment of the clumped isotope thermometer. We thank A. Templeton and L. Mayhew for XANES work on listvenite. We thank Bjørn Jamtveit (Associate Editor), Gaëlle Plissart, and an anonymous reviewer for their constructive comments, which greatly improved this paper. This work was supported by research grants to Peter Kelemen and co-workers from the National Science Foundation (EAR-1049905) and the Department of Energy (DE-FE0002386) and by a National Science Foundation Graduate Research Fellowship (DGE-07-0742).

APPENDIX A. SUPPLEMENTARY DATA

Supplementary data associated with this article can be found, in the online version, at <http://dx.doi.org/10.1016/j.gca.2015.03.014>.

REFERENCES

- Andrew K. (1985) Fluid inclusion and chemical studies of gold-quartz veins in the Atlin Camp, Northwestern British Columbia. B.Sc. thesis, Univ. British Columbia, Vancouver, BC, Canada. 116 pp.
- Bebout G. E. (2013) Metasomatism in subduction zones of subducted oceanic slabs, mantle wedges, and the slab-mantle interface. In *Metasomatism and the Chemical Transformation of Rock: The Role of Fluids in Terrestrial and Extraterrestrial Processes* (eds. D. E. Harlov and H. Austrheim). Springer, pp. 289–349.
- Beinlich A., Plümper O., Hövelmann J., Austrheim H. and Jamtveit B. (2012) Massive serpentinite carbonation at Linnajavri, N-Norway. *Terra Nova* **24**, 446–455. <http://dx.doi.org/10.1111/j.1365-3121.2012.01083.x>.
- Bond G. C. and Komazin M. A. (1984) Construction of tectonic subsidence curves for the early Paleozoic miogeocline, southern Canadian Rocky Mountains – implications for subsidence mechanisms, age of breakup, and crustal thinning. *Geol. Soc. Am. Bull.* **95**, 155–173. [http://dx.doi.org/10.1130/0016-7606\(1984\)95<155:cotscf>2.0.co;2](http://dx.doi.org/10.1130/0016-7606(1984)95<155:cotscf>2.0.co;2).
- Boudier F. and Coleman R. G. (1981) Cross section through the peridotite in the Semail ophiolite. *J. Geophys. Res.* **86**, 2573–2592.
- Boudier F., Baronnet A. and Mainprice D. (2010) Serpentine mineral replacements of natural olivine and their seismic implications: oceanic lizardite versus subduction-related antigorite. *J. Petrol.* **51**, 495–512.
- Brandenburg K. and Putz H. (2009) MATCH! – Phase Identification From Powder Diffraction Data – Version 1.9 software manual. <<http://www.crystalimpact.com>>.
- Bristow T. F., Bonifacie M., Derkowski A., Eiler J. M. and Grotzinger J. P. (2011) A hydrothermal origin for isotopically anomalous cap dolostone cements from south China. *Nature* **474**, 68–71. <http://dx.doi.org/10.1038/nature10096>.
- Buisson G. and Leblanc M. (1987) Gold in mantle peridotites from upper proterozoic ophiolites in Arabia, Mali, and Morocco. *Econ. Geol.* **82**, 2091–2097.
- Chacko T. and Deines P. (2008) Theoretical calculation of oxygen isotope fractionation factors in carbonate systems. *Geochim. Cosmochim. Acta* **72**, 3642–3660.
- Chizmeshya A. V. G., McKelvy M. J., Squires K., Carpenter R. W. and Béarat H. (2007) DOE Final Report 924162: A Novel Approach to Mineral Carbonation: Enhancing Carbonation While Avoiding Mineral Pretreatment Process Cost.
- Cipolli F., Gambardella B., Marini L., Ottonello G. and Zuccolini M. V. (2004) Geochemistry of high-pH waters from serpentinites of the Gruppo di Voltri (Genova, Italy) and reaction path modeling of CO₂ sequestration in serpentinite aquifers. *Appl. Geochem.* **19**, 787–802.
- Coto B., Martos C., Peña J. L., Rodríguez R. and Pastor G. (2012) Effects in the solubility of CaCO₃: experimental study and model description. *Fluid Phase Equilib.* **324**, 1–7.
- Das Sharma S., Patil D. J. and Gopalan K. (2002) Temperature dependence of oxygen isotope fractionation of CO₂ from magnesite-phosphoric acid reaction. *Geochim. Cosmochim. Acta* **66**, 589–593.
- Deelman J. C. (1999) Low-temperature nucleation of magnesite and dolomite. *Neues Jahrbuch Fur Mineralogie-Monatshefte* **7**, 289–302.
- Dennis K. J. and Schrag D. P. (2010) Clumped isotope thermometry of carbonatites as an indicator of diagenetic alteration. *Geochim. Cosmochim. Acta* **74**, 4110–4122. <http://dx.doi.org/10.1016/j.gca.2010.04.005>.
- Dennis K. J., Affek H. P., Passey B. H., Schrag D. P. and Eiler J. M. (2011) Defining an absolute reference frame for ‘clumped’ isotope studies of CO₂. *Geochim. Cosmochim. Acta* **75**, 7117–7131. <http://dx.doi.org/10.1016/j.gca.2011.09.025>.
- Dolejs D. and Manning C. E. (2010) Thermodynamic model for mineral solubility in aqueous fluids: theory, calibration and application to model fluid-flow systems. *Geofluids* **10**, 20–40.
- Eiler J. M. (2011) Paleoclimate reconstruction using carbonate clumped isotope thermometry. *Quat. Sci. Rev.* **30**, 3575–3588.
- Eiler J. M. and Schauble E. (2004) (OCO)-O-18-C-13-O-16 in Earth’s atmosphere. *Geochim. Cosmochim. Acta* **68**, 4767–4777. <http://dx.doi.org/10.1016/j.gca.2004.05.035>.
- Evans B. W. and Frost B. R. (1975) Chrome-spinel in progressive metamorphism – a preliminary analysis. *Geochim. Cosmochim. Acta* **39**, 959–972. [http://dx.doi.org/10.1016/0016-7037\(75\)90041-1](http://dx.doi.org/10.1016/0016-7037(75)90041-1).
- Ferry J. M., Rumble D., Wing B. A. and Penniston-Dorland S. C. (2005) A new interpretation of centimetre-scale variations in the progress of infiltration-driven metamorphic reactions: case study of carbonated metaperidotite, Val d’Efra, Central Alps, Switzerland. *J. Petrol.* **46**, 1725–1746. <http://dx.doi.org/10.1093/petrology/egi034>.
- Frezza M. L., Selverstone J., Sharp Z. D. and Compagnoni R. (2011) Carbonate dissolution during subduction revealed by diamond-bearing rocks from the Alps. *Nat. Geosci.* **4**, 703–706. <http://dx.doi.org/10.1038/ngeo1246>.

- Friedman I. and O'Neil J. R. (1977) Compilation of stable isotope fractionation factors of geochemical interest. In *USGS Prof. Paper 440-KK, Data of Geochemistry* (ed. M. Fleischer). U.S. Geological Survey, Reston, VA, KK1-KK12.
- Gherbert-Gaillard, L. (2002) Caractérisation géochimique des peridotites de l'ophiolite d'Oman: Processus magmatiques aux limites lithosphère/aesthenosphere. Ph.D. thesis, Université de Montpellier II, Montpellier, France. 217 pp.
- Ghent E. D. and Stout M. Z. (1981) Metamorphism at the base of the Samail ophiolite, southeastern Oman Mountains. *J. Geophys. Res.* **86**, 2557–2571. <http://dx.doi.org/10.1029/JB086iB04p02557>.
- Ghosh P., Adkins J., Affek H., Balta B., Guo W., Schauble E. A., Schrag D. and Eiler J. M. (2006) ^{13}C – ^{18}O bonds in carbonate minerals: a new kind of paleothermometer. *Geochim. Cosmochim. Acta* **70**, 1439–1456.
- Glennie K. W., Bouef M. G. A., Hughes-Clarke M. W., Moody-Stuart M., Pilaar W. F. H. and Reinhardt B. M. (1974) Geology of the Oman Mountains. *Verh. K. Ned. Geol. Mijnbouwk. Genoot* **31**.
- Godard M., Jousselin D. and Bodinier J.-L. (2000) Relationships between geochemistry and structure beneath a palaeo-spreading centre: a study of the mantle section in the Oman ophiolite. *Earth Planet. Sci. Lett.* **180**, 133–148.
- Gorman P. J., Kerrick D. M. and Connolly J. A. D. (2006) Modeling open system metamorphic decarbonation of subducting slabs. *Geochem. Geophys. Geosyst.* **7**, Q04007. <http://dx.doi.org/10.1029/2005gc001125>.
- Gottschalk M. (1997) Internally consistent thermodynamic data for rock-forming minerals in the system SiO_2 – TiO_2 – Al_2O_3 – Fe_2O_3 – CaO – MgO – FeO – K_2O – Na_2O – H_2O – CO_2 . *Eur. J. Mineral.* **9**, 175–223.
- Guo W. F., Mosenfelder J. L., Goddard W. A. and Eiler J. M. (2009) Isotopic fractionations associated with phosphoric acid digestion of carbonate minerals: insights from first-principles theoretical modeling and clumped isotope measurements. *Geochim. Cosmochim. Acta* **73**, 7203–7225. <http://dx.doi.org/10.1016/j.gca.2009.05.071>.
- Hacker B. R., Mosenfelder J. L. and Gnos E. (1996) Rapid emplacement of the Oman ophiolite: thermal and geochronologic constraints. *Tectonics* **15**, 1230–1247. <http://dx.doi.org/10.1029/96tc01973>.
- Haggerty J. A. (1991) Evidence from fluid seeps atop serpentine seamounts in the Mariana Forearc: clues for emplacement of the seamounts and their relationship to forearc tectonics. *Mar. Geol.* **102**, 293–309.
- Halls C. and Zhao R. (1995) Listvenite and related rocks: perspectives on terminology and mineralogy with reference to an occurrence at Cregganbaun, Co., Mayo, Republic of Ireland. *Miner. Deposita* **30**, 303–313.
- Hänchen M., Prigiobbe V., Baciocchi R. and Mazzotti M. (2008) Precipitation in the Mg-carbonate system: effects of temperature and CO_2 pressure. *Chem. Eng. Sci.* **63**, 1012–1028.
- Hanghøj K., Kelemen P. B., Hassler D. and Godard M. (2010) Composition and genesis of depleted mantle peridotites from the Wadi Tayin Massif, Oman Ophiolite; major and trace element geochemistry, and Os isotope and PGE systematics. *J. Petrol.* **51**, 201–227. <http://dx.doi.org/10.1093/petrology/egp077>.
- Hansen L. D., Dipple G. M., Gordon T. M. and Kellett D. A. (2005) Carbonated serpentinite (listwanite) at Atlin, British Columbia: a geological analogue to carbon dioxide sequestration. *Can. Mineral.* **43**, 225–239.
- Hensen C., Wallmann K., Schmidt M., Ranero C. R. and Suess E. (2004) Fluid expulsion related to mud extrusion off Costa Rica – A window to the subducting slab. *Geology* **32**, 201–204. <http://dx.doi.org/10.1130/g20119.1>.
- Holland T. J. B. and Powell R. (1998) An internally consistent thermodynamic data set for phases of petrological interest. *J. Metamorph. Geol.* **16**, 309–343.
- Holland T. J. B. and Powell R. (2011) An improved and extended internally consistent thermodynamic dataset for phases of petrological interest, involving a new equation of state for solids. *J. Metamorph. Geol.* **29**, 333–383. <http://dx.doi.org/10.1111/j.1525-1314.2010.00923.x>.
- Huntington K. W., Eiler J. M., Affek H. P., Guo W., Bonifacie M., Yeung L. Y., Thiagarajan N., Passey B., Tripathi A., Daëron M. and Came R. (2009) Methods and limitations of 'clumped' CO_2 isotope ($\Delta 47$) analysis by gas-source isotope ratio mass spectrometry. *J. Mass Spectrom.* **44**, 1318–1329. <http://dx.doi.org/10.1002/jms.1614>.
- Jamtveit B., Malthes-Sørenssen A. and Kostenko O. (2008) Reaction enhanced permeability during retrogressive metamorphism. *Earth Planet. Sci. Lett.* **267**, 620–627.
- Jamtveit B., Putnis C. and Malthes-Sørenssen A. (2009) Reaction induced fracturing during replacement processes. *Contrib. Mineral. Petrol.* **157**, 127–133.
- Johnson J. W., Oelkers E. H. and Helgeson H. C. (1992) SUPCRT92: a software package for calculating the standard molal thermodynamic properties of minerals, gases, aqueous species, and reactions from 1 to 5000 bars and 0 to 1000 °C. *Comput. Geosci.* **18**, 899–947.
- Kelemen P. B. and Hirth G. (2012) Reaction-driven cracking during retrograde metamorphism: olivine hydration and carbonation. *Earth Planet. Sci. Lett.* **345**, 81–89. <http://dx.doi.org/10.1016/j.epsl.2012.06.018>.
- Kelemen P. B. and Manning C. E. (2015) Re-evaluating carbon fluxes in subduction zones: What goes down, mostly comes up. *Proc. Natl. Acad. Sci. U.S.A.*
- Kelemen P. B. and Matter J. M. (2008) In situ carbonation of peridotite for CO_2 storage. *Proc. Natl. Acad. Sci. U.S.A.* **105**, 17295–17300.
- Kelemen P. B., Matter J., Streit E. E., Rudge J. F., Curry W. B. and Bluztajn J. (2011) Rates and mechanisms of mineral carbonation in peridotite: natural processes and recipes for enhanced, in situ CO_2 capture and storage. *Annu. Rev. Earth Planet. Sci.* **39**, 545–576.
- Kerrick D. M. and Connolly J. A. D. (2001) Metamorphic devolatilization of subducted marine sediments and the transport of volatiles into the Earth's mantle. *Nature* **411**, 293–296. <http://dx.doi.org/10.1038/35077056>.
- Kim S. T. and O'Neil J. R. (1997) Equilibrium and nonequilibrium oxygen isotope effects in synthetic carbonates. *Geochim. Cosmochim. Acta* **61**, 3461–3475.
- Kimball K. (1990) Effects of hydrothermal alteration on the compositions of chromian spinels. *Contrib. Mineral. Petrol.* **105**, 337–346.
- Klein F. and Garrido C. J. (2011) Thermodynamic constraints on mineral carbonation of serpentinitized peridotite. *Lithos* **126**, 147–160.
- Konno U., Tsunogai U., Nakagawa F., Nakaseama M., Ishibashi J., Nunoura T. and Nakamura K. (2006) Liquid CO_2 venting on the seafloor: Yonaguni Knoll IV hydrothermal system, Okinawa Trough. *Geophys. Res. Lett.* **33**. <http://dx.doi.org/10.1029/2006GL026115>.
- Lackner K. S., Wendt C. H., Butt D. P., Joyce E. L. and Sharp D. H. (1995) Carbon-dioxide disposal in carbonate minerals. *Energy* **20**, 1153–1170.
- Lippard S. J., Shelton A. W. and Gass I. G. (1986) *The ophiolite of Northern Oman. Geological Society of London, Memoir 11*. Blackwell Scientific Publications, London.

- Ludwig K. R. (2003) Mathematical-statistical treatment of data and errors for Th-230/U geochronology. Uranium-series geochemistry. *Rev. Mineral. Geochem.* **52**, 631–656.
- Lupton J., Butterfield D., Lilley M., Evans L., Nakamura K., Chadwick W., Resing J., Embley R., Olson E., Proskurowski G., Baker E., de Ronde C., Roe K., Greene R., Lebon G. and Young C. (2006) Submarine venting of liquid carbon dioxide on a Mariana Arc volcano. *Geochem. Geophys. Geosyst.* **7**, Q08007.
- Lynch F. L. (1997) Frio shale mineralogy and the stoichiometry of the smectite-to-illite reaction: the most important reaction in clastic sedimentary diagenesis. *Clay Clay Miner.* **45**, 618–631. <http://dx.doi.org/10.1346/ccmn.1997.0450502>.
- MacDonald A. H. and Fyfe W. S. (1985) Rate of serpentinization in seafloor environments. *Tectonophysics* **116**, 123–135.
- Madu B. E., Nesbitt B. E. and Muehlenbachs K. (1990) A mesothermal gold-stibnite-quartz vein occurrence in the Canadian Cordillera. *Econ. Geol.* **85**, 1260–1268.
- Mellini M., Rumori C. and Viti C. (2005) Hydrothermally reset magmatic spinels in retrograde serpentinites: formation of “ferritchromit” rims and chlorite aureoles. *Contrib. Mineral. Petrol.* **149**, 266–275.
- Mottl M. J., Wheat G., Fryer P., Gharib J. and Martin J. B. (2004) Chemistry of springs across the Mariana forearc shows progressive devolatilization of the subducting plate. *Geochim. Cosmochim. Acta* **68**, 4915–4933.
- Nasir S., Al Sayigh A. R., Al Harthy A., Al-Khirbush S., Al-Jaaidi O., Musllam A., Al-Mishwat A. and Al-Bu'saidi S. (2007) Mineralogical and geochemical characterization of listwaenite from the Semail ophiolite, Oman. *Chem. Erde-Geochem.* **67**, 213–228.
- Nicolas A., Boudier E., Ildefonse B. and Ball E. (2000) Accretion of Oman and United Arab Emirates ophiolite: discussion of a new structural map. *Mar. Geophys. Res.* **21**, 147–179.
- O'Connor W. K., Dahlin D. C., Rush G. E., Gerdemann S. J. and Nilsen D. N. (2005) Aqueous mineral carbonation, Final Report DOE/ARC-TR-04-002. Office of Process Development, Albany Research Center, Office of Fossil Energy, U.S. Dept. Energy, Albany, OR.
- Oskierski H. C., Bailey J. G., Kennedy E. M., Jacobsen G., Ashley P. M. and Dlugogorski B. Z. (2013) Formation of weathering-derived magnesite deposits in the New England Orogen, New South Wales, Australia: implications from mineralogy, geochemistry and genesis of the Attunga magnesite deposit. *Miner. Deposita* **48**, 525–541. <http://dx.doi.org/10.1007/s00126-012-0440-5>.
- Passey B. H., Levin N. E., Cerling T. E., Brown F. H. and Eiler J. M. (2010) High-temperature environments of human evolution in East Africa based on bond ordering in paleosol carbonates. *Proc. Natl. Acad. Sci. U.S.A.* **107**, 11245–11249. <http://dx.doi.org/10.1073/pnas.1001824107>.
- Petschick R. (2001) MacDiff 4.2.5 Software Manual. <<http://www.geol-pal.uni-frankfurt.de/Staff/Homepages/Petschick/MacDiff/MacDiffInfoE.html>>.
- Plank T. and Langmuir C. H. (1998) The chemical composition of subducting sediment and its consequences for the crust and mantle. *Chem. Geol.* **145**, 325–394. [http://dx.doi.org/10.1016/S0009-2541\(97\)00150-2](http://dx.doi.org/10.1016/S0009-2541(97)00150-2).
- Plissart G., Femenias O., Maruntiu M., Diot H. and Demaiffe D. (2009) Mineralogy and geothermometry of gabbro-derived listvenites in the Tisovita-Iuti Ophiolite, southwestern Romania. *Can. Mineral.* **47**, 81–105.
- Plümper O., Røyne A., Magrasó A. and Jamtveit B. (2012) The interface-scale mechanism of reaction-induced fracturing during serpentinization. *Geology* **40**, 1103–1106.
- Power I. M., Wilson S. A., Harrison A. L., Dipple G. M., McCutcheon J., Southam G. and Kenward P. A. (2014) A depositional model for hydromagnesite–magnesite playas near Atlin, British Columbia, Canada. *Sedimentology* **61**, 1701–1733.
- Rioux M., Bowring S., Kelemen P., Gordon S., Miller R. and Dudas F. (2013) Tectonic development of the Semail ophiolite: high-precision U-Pb zircon geochronology and Sm-Nd isotopic constraints on crustal growth and emplacement. *J. Geophys. Res. Solid Earth* **118**, 2085–2101. <http://dx.doi.org/10.1002/jgrb.50139>.
- Rose G. (1837) Mineralogisch-geognostische Reise nach dem Ural, dem Altai und dem Kaspischen Meere. In *Reise nach dem nördlichen Ural und dem Altai*, Volume 1 (ed. G. E. Reimer). Verlag der Sanderschen Buchhandlung, Berlin.
- Rudge J. F., Kelemen P. B. and Spiegelman M. (2010) A simple model of reaction-induced cracking applied to serpentinization and carbonation of peridotite. *Earth Planet. Sci. Lett.* **291**, 215–227.
- Rüpke L. H., Morgan J. P., Hort M. and Connolly J. A. D. (2004) Serpentine and the subduction zone water cycle. *Earth Planet. Sci. Lett.* **223**, 17–34. <http://dx.doi.org/10.1016/j.epsl.2004.04.018>.
- Sakai H., Gamo T., Kim E.-S., Tsutsumi M., Tanaka T., Ishibashi J., Wakita H., Yamano M. and Oomori T. (1990) Venting of carbon dioxide-rich fluid and hydrate formation in Mid-Okinawa Trough backarc basin. *Science* **248**, 1093–1098.
- Saldi G. D., Schott J., Pokrovsky O. S. and Oelkers E. H. (2010) An experimental study of magnesite dissolution rates at neutral to alkaline conditions and 150 and 200 °C as a function of pH, total dissolved carbonate concentration, and chemical affinity. *Geochim. Cosmochim. Acta* **74**, 6344–6356. <http://dx.doi.org/10.1016/j.gca.2010.07.012>.
- Saldi G. D., Schott J., Pokrovsky O. S., Gautier Q. and Oelkers E. H. (2012) An experimental study of magnesite precipitation rates at neutral to alkaline conditions and 100–200 °C as a function of pH, aqueous solution composition and chemical affinity. *Geochim. Cosmochim. Acta* **83**, 93–109. <http://dx.doi.org/10.1016/j.gca.2011.12.005>.
- Schandl E. S. and Gorton M. P. (2012) Hydrothermal alteration and CO₂ metasomatism (natural carbon sequestration) of komatiites in the south-western Abitibi greenstone belt. *Can. Mineral.* **50**, 129–146. <http://dx.doi.org/10.3749/canmin.50.1.129>.
- Schandl E. S. and Wicks F. J. (1993) Carbonate and associated alteration of ultramafic and rhyolitic rocks at the Hemingway Property, Kidd Creek Volcanic Complex, Timmins, Ontario. *Econ. Geol.* **88**, 1615–1635.
- Schauble E. A., Ghosh P. and Eiler J. M. (2006) Preferential formation of C-13-O-18 bonds in carbonate minerals, estimated using first-principles lattice dynamics. *Geochim. Cosmochim. Acta* **70**, 2510–2529. <http://dx.doi.org/10.1016/j.gca.2006.02.011>.
- Seifritz W. (1990) CO₂ disposal by means of silicates. *Nature* **345**, 486.
- Spiridonov E. M. (1991) Listvenites and zodites. *Int. Geol. Rev.* **33**, 397–407.
- Stanger G. (1985) Silicified serpentinite in the Semail nappe of Oman. *Lithos* **18**, 13–22.
- Streit E., Kelemen P. and Eiler J. (2012) Coexisting serpentine and quartz from carbonate-bearing serpentinized peridotite in the Semail ophiolite, Oman. *Contrib. Mineral. Petrol.* **164**, 821–837. <http://dx.doi.org/10.1007/s00410-012-0775-z>.
- Syracuse E. M., van Keken P. E. and Abers G. A. (2010) The global range of subduction zone thermal models. *Phys. Earth Planet. Inter.* **183**, 73–90.
- Templeton A. S., Knowles E. J., Eldridge D. L., Arey B. W., Dohnalkova A., Webb S. M., Bailey B. E., Tebo B. M. and Staudigel H. S. (2009) A seafloor microbial biome hosted within

- incipient ferromanganese crusts. *Nat. Geosci.* **2**, 872–876. <http://dx.doi.org/10.1038/ngeo696>.
- Toner B., Berquó T., Michel M., Templeton A. S., Sorenson J. V. and Edwards K. J. (2012) Mineralogy of iron microbial mats from Loihi Seamount. *Front. Microbiol.* **3**. <http://dx.doi.org/10.3389/fmicb.2012.00118>.
- Trommsdorff V. and Evans B. W. (1972) Progressive metamorphism of antigorite schists in the Bergell tonalite aureole (Italy). *Am. J. Sci.* **272**, 423–437.
- Vasconcelos C., McKenzie J. A., Warthmann R. and Bernasconi S. M. (2005) Calibration of the $d^{18}\text{O}$ paleothermometer for dolomite precipitated in microbial cultures and natural environments. *Geology* **33**, 317–320.
- Veizer J., Ala D., Azmy K., Bruckschen P., Buhl D., Bruhn F., Carden G. A. F., Diener A., Ebner S., Godderis Y., Jasper T., Korte C., Pawellek F., Podlaha O. G. and Strauss H. (1999) $^{87}\text{Sr}/^{86}\text{Sr}$, $\delta^{13}\text{C}$ and $\delta^{18}\text{O}$ evolution of Phanerozoic seawater. *Chem. Geol.* **161**, 59–88.
- Villey M., Le Métour J. and de Gramont X. (1986) Geological Map of Fanjah. Muscat, Oman, Ministry of Petroleum and Minerals, Directorate General of Minerals, Sultanate of Oman.
- Wallmann K. (2001) Controls on the cretaceous and cenozoic evolution of seawater composition, atmospheric CO_2 and climate. *Geochim. Cosmochim. Acta* **65**, 3005–3025. [http://dx.doi.org/10.1016/s0016-7037\(01\)00638-x](http://dx.doi.org/10.1016/s0016-7037(01)00638-x).
- Wang Z. G., Schauble E. A. and Eiler J. M. (2004) Equilibrium thermodynamics of multiply substituted isotopologues of molecular gases. *Geochim. Cosmochim. Acta* **68**, 4779–4797.
- Weir R. H. and Kerrick D. M. (1987) Mineralogic, fluid inclusion, and stable isotope studies of several gold-mines in the Mother Lode, Tuolumne and Mariposa Counties, California. *Econ. Geol.* **82**, 328–344.
- Weyhenmeyer C. E. (2000) Origin and evolution of groundwater in the alluvial aquifer of the eastern Batinah coastal plain, Sultanate of Oman: a hydrogeochemical approach. Ph.D. thesis, Universität Bern, Bern, Switzerland.
- Wilde A., Simpson L. and Hanna S. (2002) Preliminary study of Cenozoic alteration and platinum deposition in the Oman ophiolite. *J. Virtual Explorer* **6**, 7–13.
- Wolery T.J. (1992). EQ3/6, A Software Package for Geochemical Modeling of Aqueous Systems: Package Overview and Installation Guide (Version 7.0). Lawrence Livermore National Laboratory, Livermore, CA.
- Xu W. Y., Apps J. A. and Pruess K. (2004) Numerical simulation of CO_2 disposal by mineral trapping in deep aquifers. *Appl. Geochem.* **19**, 917–936.

Associate editor: Bjorn Jamtveit

Geochemistry and petrology of listvenite in the Samail Ophiolite, Sultanate of Oman: Complete carbonation of peridotite during ophiolite emplacement

Elisabeth S. Falk and Peter B. Kelemen

Supplementary text

Section S.1 Other carbonated peridotite lithologies in Oman

Section S.2 Clumped isotope analysis of magnesite

Section S.3 Bulk compositions and element mobility

Section S.4 Oxygen isotopes in carbonate and quartz

References cited in Electronic Supplement

List of Supplementary Tables

Supplementary Figure Captions

Supplementary Figures

S1. Other carbonated peridotite lithologies in Oman

We collected the listvenite and nearby metasediments and serpentinized peridotite samples discussed here in January of 2009, 2010, and 2011. During these field seasons, we also collected other products of peridotite carbonation, including low-temperature carbonate-veined serpentinite, travertine formed at alkaline springs associated with ongoing serpentinization, and other highly carbonated ultramafic lithologies such as magnesite-talc soapstones. Our results indicate that carbonation of peridotite in Oman has occurred over wide range of time scales, environments, and temperatures (from ~30°C in carbonate-veined serpentinites (Streit et al., 2012) to >300°C in magnesite-talc soapstones). Distinct mineral assemblages and patterns of iron partitioning between Mg-

silicates and carbonate minerals are observed for different temperature regimes.

At Wadi Abyad (568250E, 259300N UTM zone 40Q), we find highly carbonated peridotites composed primarily of magnesite + talc \pm serpentine, in localized, centimeter- to meter-scale zones within serpentinitized peridotite (Supplementary Figure S1). Without quartz, and with some Mg remaining in silicate phases rather than in carbonates, these “soapstones” are not listvenites following the definition of Halls and Zhao (1995), but fall within a spectrum of carbonated peridotite alteration products formed at depth that includes true listvenites. These rocks appear unrelated to the formation of listvenite discussed here and do not have equivalents in the active carbonation systems observed in Oman today (Streit et al., 2012; Kelemen et al., 2011).

Clumped isotope analysis of magnesite from soapstone sample OM11-94 from Wadi Abyad yielded $\Delta 47$ values of $0.347 \pm 0.017\text{‰}$ (ARF) corresponding to a clumped isotope temperature of $\sim 300^\circ\text{C}$ using the polynomial $\Delta 47$ -temperature calibration of Bristow et al. (2011). It is possible that this magnesite formed at significantly higher temperatures than this, as the $\Delta 47$ of magnesite in this sample was even lower than that recorded by magnesite formed at $\sim 645^\circ\text{C}$ during regional metamorphism of peridotite in Val d'Efra $645 \pm 10^\circ\text{C}$ (Ferry et al., 2005), which yielded a closure temperature or a closure temperature, of $\sim 213^\circ\text{C}$ using the polynomial $\Delta 47$ -temperature calibration of Bristow et al. (2011) (see Supplementary section S2, Table S2, and Figure S4). This higher temperature for magnesite coexisting with talc without serpentine is consistent with the fact that magnesite + talc is stable over a wider range of fluid compositions at higher temperature. $\delta^{18}\text{O}$ values in magnesite from this sample, $12.7 \pm 0.1\text{‰}$ (SMOW),

are also much lower than those measured in listvenite, consistent with a high-temperature origin.

Supplementary Figure S2 shows the distribution of iron in magnesium silicates and carbonates for low-temperature carbonate veined serpentinites, listvenites and listvenite-transitional lithologies, and zoned magnesite-talc soapstones from Oman. Streit et al. (2012) noted that serpentine in carbonate-veined peridotite in the Oman ophiolite was generally more iron-rich than lizardite from serpentinized peridotite from the literature (Evans et al., 2009), and that this may indicate low temperature serpentinization accompanied carbonate vein formation during near-surface alteration by groundwater at temperatures of $\sim 40^{\circ}\text{C}$. Comparing the low-temperature system with listvenite-transitional serpentinites and listvenites (clumped isotope temperatures $\sim 90^{\circ}\text{C}$) and zoned magnesite-talc soapstone (clumped isotope temperature $> 300^{\circ}\text{C}$), we see that iron content in serpentine is highest in the low temperature system ($\sim 8\%$ molar $\text{Fe}/(\text{Fe}+\text{Mg})$), decreases to a molar $\text{Fe}/(\text{Fe}+\text{Mg})$ of $\sim 4\%$ for listvenite-transitional serpentinites, and is lowest in the magnesite-talc soapstones (molar $\text{Fe}/(\text{Fe}+\text{Mg}) \sim 3\%$). Meanwhile, the iron Fe content of magnesite increase from low temperature samples to higher temperature samples, with molar $\text{Fe}/(\text{Fe}+\text{Mg})$ of only $\sim 1\%$ in low-temperature magnesite veins, molar $\text{Fe}/(\text{Fe}+\text{Mg})$ around 5% in listvenites, a broad range of iron content in the magnesite-talc soapstones ranging from $\sim 5\text{-}15\%$ molar $\text{Fe}/(\text{Fe}+\text{Mg})$.

Given that carbonation and hydration of peridotite can take place over a wide range of conditions, it is unsurprising that evidence of multiple episodes of alteration can be found in some samples. For example, in some of the partially serpentinized samples near the listvenite in Wadi Mansah, the mesh is defined by the $\text{Mg}\# \sim 95$ serpentine typical of

this area, but more Fe-rich serpentine (e.g., Mg# ~85) rims or completely replaces relict olivine in the mesh cores, and account for ~10% of the serpentine present in these samples (Supplementary Figure S3). These limited amounts of low-Mg# serpentine likely represent later, lower-temperature alteration (Streit et al., 2012) superimposed on pre- and syn-obduction serpentinization and suggest that even more olivine may have been available for reaction in the listvenite protolith than is observed as relicts in the partially serpentinized peridotite in this area today. Minor precipitation of carbonates and/or recrystallization could also have occurred during low temperature, post-emplacement interaction with groundwater, and may account for some of the lower carbonate clumped isotope temperatures derived from some listvenites.

S.2 Clumped isotope analysis of magnesite formed at known temperatures

Synthetic magnesite grown at temperatures of 120-250°C and natural playa magnesite formed at temperatures of 3-10°C agree well with the quadratic relationship between $\Delta 47$ and $10^6/T^2$ implied by the data of Bristow et al. (2011), also collected at Caltech, projected into the absolute reference frame using their calcite standard data. These data suggest that there are not significant differences between clumped isotope thermometers for different minerals, and that the interlaboratory discrepancies observed for low temperature calcites exist for other carbonate minerals as well and are not related differences in acid digestion methods.

Three magnesite samples were plotted separately (red x's in Figure S4) because of high temperatures of formation exceeding likely closure temperatures, uncertain temperature of formation, or uncertain mineralogy. Magnesite from a metaperidotite

sample from Val d'Efra records a $\Delta 47$ value of 0.387‰, corresponding to a "closure" temperature of 213°C using the calibration of Bristow et al. (2011), much lower than the 645°C experienced by the rock during regional metamorphism (Ferry et al. 2005), but similar to closure temperatures inferred from contact metamorphosed dolomite marbles (Ferry et al. 2011), carbonatites (Dennis and Schrag 2010), and slowly cooled marbles (Ghosh et al. 2006). The temperature of formation of magnesite from listvenite from Atlin, British Columbia (210-280°C) was constrained from fluid inclusions in quartz published in a B.Sc. thesis (Andrew, 1985), and there is some uncertainty whether these quartz fluid inclusion temperatures accurately reflect magnesite precipitation temperatures in these rocks. The "magnesite" grown at 40°C reacted vigorously with acid even at room temperature and magnesite-like peaks in its XRD pattern were slightly shifted from expected 2-theta values. Attempts to remove co-existing dolomite and calcite using dilute HCl may have effected the isotopic signature of the remaining "magnesite."

Based on these results of clumped isotope analysis of magnesite formed at known temperatures, the calibration employed by Bristow et al. (2011) was used in reporting clumped isotope temperatures for all samples in the main text. Results of clumped isotope thermometry using other calibrations are available as well in Supplementary Table S2, which presents all clumped isotope measurements, including Oman samples, known-temperature magnesite samples, standards, and heated gases. All $\Delta 47$ values discussed in the main text and supplementary information have been converted to the absolute reference frame of Dennis et al. (2011) using a transfer function derived from heated gases and calcite standards (Supplementary Table S3).

S.3. Bulk compositions and element mobility in listvenite

Volatile-free major and trace element bulk compositions of magnesite-quartz listvenites from the Wadi Mansah locality (Supplementary Table S4) are frequently the same, within error, as average Oman harzburgite for all elements for which our XRF data can be compared with the data from Hanghøj et al. (2010), as shown in several selected modified isocon plots in Supplementary Figure S5. By contrast, dolomite-quartz listvenite bulk compositions are highly enriched in calcium and depleted in magnesium, and show variable addition or loss of other major and trace elements, such that no samples are the same, within error, as the bulk composition of average harzburgite even when projected from Ca and CO₂.

Components commonly considered to be immobile during hydrothermal alteration, such as Ti, Al, and Cr, can vary in concentration by up to more than an order of magnitude in Oman listvenites, and frequently do not overlap the 2- σ natural compositional variability in Oman harzburgite compositions reported by Hanghøj et al. (2010), as plotted in the modified isocons in Supplementary Figure S5. Although they are positively correlated, changes in Ti and Al are not proportional in a way that can be explained by losses or gains in other components and therefore suggest either mobility during hydrothermal alteration or greater local variability in the harzburgite protolith than that documented by Hanghøj et al. (2010). For example, if apparent losses in Ti and Al in the modified isocons in Supplementary Figure S5 were assumed to be due to volume changes, it would require that huge amounts of Fe, Mg, and Si were added to the rock without altering their relative proportions. Figure 7 illustrates that there is almost as much

variability in these minor elements in local partially serpentinized peridotite and fresh Oman peridotite (Godard et al., 2000; Hanghøj et al., 2010) as in the listvenites.

Overall, bulk compositions approximate fresh Oman peridotite with the addition of CO₂ and in the case dolomite, Ca replacement of Mg. Redistribution of components within the outcrop results in apparent losses and additions the hand sample scale, but does not appear to result in net transport of materials into or out of the system. At the sample scale, Si and Mg is observed to be mobilized and redistributed in abundant quartz veins and carbonate veins extending from micrometer to centimeter scales. Hydrothermal alteration has also modified the composition of relict Cr-spinel (Supplementary Table S11). While partially serpentinized peridotites near the listvenite bands contain relatively MgAl₂O₄-rich Cr-spinel end-members typical of Oman harzburgite (Hanghøj et al., 2010), most spinels from listvenite samples have much lower Mg# (molar Mg/(Mg+Fe)) and higher Cr# (molar Cr/(Cr+Al)) (Supplementary Table S11). In one magnesite-quartz listvenite, Cr-spinel relicts are absent and have been completely replaced with the Cr-mica fuchsite (see BSE image in Supplementary Figure S6). Mg# and Cr# in fuchsite in this sample fall along the range between unaltered spinels in partially serpentinized peridotites and altered spinels in listvenites (Supplementary Figure S7).

S4. $\delta^{18}\text{O}$ in quartz and carbonate from listvenite

Carbonate $\delta^{18}\text{O}$ values obtained during clumped isotope analyses are provided in Table 2 and Supplementary Table S2. Quartz $\delta^{18}\text{O}$ values are presented in Supplementary Table S5.

Quartz and magnesite $\delta^{18}\text{O}$ values are positively correlated (Figure 11), but quartz-carbonate fractionation factors cannot be reliably used to independently estimate temperatures and oxygen isotopic compositions of the fluid in our samples. Quartz appears to be in isotopic equilibrium with magnesite, but the temperature dependence of magnesite-quartz fractionation factors is weak and non-monotonic when calculated using the reduced partition function ratios for magnesite of Chacko and Deines (2008) or Schauble et al. (2006). Although we cannot use quartz-magnesite $\delta^{18}\text{O}$ fractionation to derive precipitation temperatures, the fact that the two phases appear to be in isotopic equilibrium is another indication, in addition to textural and compositional evidence, that magnesite and quartz co-precipitated.

Quartz and dolomite $\delta^{18}\text{O}$ values are also positively correlated, but at least some samples appear to be out of quartz-dolomite exchange equilibrium. Quartz has lower $\delta^{18}\text{O}$ than dolomite in all four dolomite-quartz listvenite samples in which we analyzed quartz, in contrast to mostly positive quartz-dolomite fractionation factors calculated using dolomite-fluid fractionation factors from Chacko and Deines (2008), Schauble et al. (2006), or Sheppard and Schwarcz (1970) and quartz-fluid fractionation factors from Friedman and O'Neil (1977) or Sharp and Kirschner (1994). Two samples had only slightly negative quartz-dolomite fractionations of -0.2‰ and -0.4‰ . These two negative values correspond to isotopic equilibration at temperatures of $\sim 90^\circ\text{C}$ using a combination of fractionation factors from Schmidt et al. (2005) and Friedman and O'Neil (1977), but require temperatures of $\sim 150^\circ\text{C}$ if quartz fractionation factors are taken from Sharp and Kirschner (1994), $\sim 200^\circ\text{C}$ if dolomite fractionation factors are taken from Vasconcelos et al. (2005), and $\sim 250\text{-}300^\circ\text{C}$ if dolomite fractionation factors are taken from Northrop and

Clayton (1966). Two samples had quartz-carbonate fractionations of -3.3‰, which is unattainable for most combinations of available dolomite and quartz fractionation factors, only being reached at temperatures in excess of 250°C for the choice of quartz-dolomite fractionation factors derived from Schmidt et al. (2005) and Friedman and O'Neil (1977). Vein dolomite in one of these samples, OM09-19, is probably out of oxygen isotopic equilibrium with groundmass magnesite, as dolomite has higher $\delta^{18}\text{O}$ than magnesite in this sample, whereas theory predicts that magnesite should always have higher $\delta^{18}\text{O}$ than dolomite (Schauble et al., 2006; Chacko and Deines 2008).

Rather than looking at carbonate-quartz oxygen isotope thermometers, it can be useful to consider how well temperature estimates from mineral-water oxygen isotope fractionation agree between samples, for carbonate versus quartz, and for different available fractionation factors at a given assumed fluid $\delta^{18}\text{O}$. Examples of the range of temperatures derived from the range of available mineral-water fractionation factors are provided in Supplementary Table S6. In general there is good overlap of temperature ranges derived from dolomite, magnesite, and quartz $\delta^{18}\text{O}$ for assumed fluid $\delta^{18}\text{O} = 0\text{‰}$. Although these calculations do not provide definitive temperatures of listvenite formation, they demonstrate that the $\delta^{18}\text{O}$ data could be consistent with formation at temperatures around 90°C from a fluid with $\delta^{18}\text{O}$ near 0‰.

Likewise, we can also look at how well the $\delta^{18}\text{O}$ of the fluid calculated from carbonate and quartz $\delta^{18}\text{O}$ values overlap for a number of available mineral-water fractionation factors over a range relevant temperatures. Such calculations are presented in Supplementary Figure S8, for temperatures of 80-130°C (range of temperatures by mineral paragenesis). Carbonate and quartz can be considered to be in isotopic equilibrium

where calculated fluid oxygen isotope values at a given temperature overlap for some choice of fractionation factors for carbonate and quartz. Oxygen isotopes in magnesite and quartz are in good agreement for most choices of fractionation factors for all samples. In dolomite listvenites, quartz and dolomite appear to be in isotopic equilibrium for some choices of fractionation factors in two out of four samples. $\delta^{18}\text{O}$ compositions of carbonate and quartz in listvenite would be in equilibrium with average fluid $\delta^{18}\text{O}$ values ranging from about $-1 \pm 3\text{‰}$ at 80°C to $5 \pm 3\text{‰}$ at 130°C .

References cited in Electronic Supplement

- Andrew K. (1985) Fluid inclusion and chemical studies of gold-quartz veins in the Atlin Camp, Northwestern British Columbia. B.Sc. thesis, Univ. British Columbia, Vancouver, B.C., Canada. 116 pp.
- Aharon P. (1988) A stable-isotope study of magnesites from the Rum Jungle Uranium Field, Australia - Implications for the origin of strata-bound massive magnesites. *Chem. Geol.* **69**, 127-145. doi:10.1016/0009-2541(88)90164-7
- Braun M. G. (2004). Petrological and microstructural constraints on focused melt transport in dunites and rheology of the shallow mantle. Ph.D. thesis, MIT-WHOI joint graduate program, Woods Hole, MA, USA. 212 pp.
- Bristow T. F., Bonifacie M., Derkowski A., Eiler J. M. and Grotzinger J. P. (2011) A hydrothermal origin for isotopically anomalous cap dolostone cements from south China. *Nature* **474**, 68-71. doi:10.1038/nature10096
- Chacko T. and Deines P. (2008) Theoretical calculation of oxygen isotope fractionation factors in carbonate systems. *Geochim. Cosmochim. Acta* **72**, 3642-3660.
- Dennis K. J. and Schrag D. P. (2010) Clumped isotope thermometry of carbonatites as an indicator of diagenetic alteration. *Geochim. Cosmochim. Acta* **74**, 4110-4122. doi:10.1016/j.gca.2010.04.005.
- Dennis K. J., Affek H. P., Passey B. H., Schrag D. P. and Eiler J. M. (2011) Defining an absolute reference frame for 'clumped' isotope studies of CO₂. *Geochim. Cosmochim. Acta* **75**, 7117-7131. doi:10.1016/j.gca.2011.09.025
- Dick H. J. B. (1989). Abyssal peridotites, very slow spreading ridges, and ocean ridge magmatism. In *Magmatism in the Ocean Basins*. (eds. Saunders A. D. and Norry M. J.) Geol. Soc., London, Special Publications **42**, 71-105.
- Evans B. W., Kuehner S. M., Chopelas A. (2009) Magnetite-free, yellow lizardite serpentinization of olivine websterite, Canyon Mountain complex, NE Oregon. *Am. Mineral.* **94**:1731-1734. doi:10.2138/am.2009.3301
- Ferry J. M., Rumble D., Wing B. A. and Penniston-Dorland S. C. (2005) A new interpretation of centimetre-scale variations in the progress of infiltration-driven metamorphic reactions: Case study of carbonated metaperidotite, Val d'Efra, Central Alps, Switzerland. *J. Petrol.* **46**, 1725-1746. doi:10.1093/petrology/egi034
- Ferry J. M., Passey B. H., Vasconcelos C. and Eiler J. M. (2011) Formation of dolomite at 40-80 degrees C in the Latemar carbonate buildup, Dolomites, Italy, from clumped isotope thermometry. *Geology* **39**, 571-574. doi:10.1130/g31845.1

- Friedman I. and O'Neil J. R. (1977) Compilation of stable isotope fractionation factors of geochemical interest. In *USGS Prof. Paper 440-KK, Data of Geochemistry* (ed. Fleischer M.) U.S. Geological Survey, Reston, VA, KK1-KK12.
- Ghosh P., Adkins J., Affek H., Balta B., Guo W., Schauble E. A., Schrag D. and Eiler J. M. (2006) ^{13}C – ^{18}O bonds in carbonate minerals: A new kind of paleothermometer. *Geochim. Cosmochim. Acta* **70**, 1439-1456.
- Godard M., Jousselein D. and Bodinier J.-L. (2000) Relationships between geochemistry and structure beneath a palaeo-spreading centre: a study of the mantle section in the Oman ophiolite. *Earth Planet. Sc. Lett.* **180**, 133-148.
- Guo W. F., Mosenfelder J. L., Goddard W. A. and Eiler J. M. (2009) Isotopic fractionations associated with phosphoric acid digestion of carbonate minerals: Insights from first-principles theoretical modeling and clumped isotope measurements. *Geochim. Cosmochim. Acta* **73**, 7203-7225.
doi:10.1016/j.gca.2009.05.071
- Halls C. and Zhao R. (1995) Listvenite and related rocks: Perspectives on terminology and mineralogy with reference to an occurrence at Cregganbaun, Co. Mayo, Republic of Ireland. *Miner. Deposita* **30**, 303-313.
- Hanghøj K., Kelemen P. B., Hassler D. and Godard M. (2010) Composition and Genesis of Depleted Mantle Peridotites from the Wadi Tayin Massif, Oman Ophiolite; Major and Trace Element Geochemistry, and Os Isotope and PGE Systematics. *J. Petrol.* **51**, 201-227. doi:10.1093/petrology/egp077
- Kelemen P. B., Matter J., Streit E. E., Rudge J. F., Curry W. B. and Bluztajn J. (2011) Rates and mechanisms of mineral carbonation in peridotite: Natural processes and recipes for enhanced, in situ CO_2 capture and storage. *Ann. Rev. Earth Pl. Sc.* **39**, 545-576.
- Northrop D. A. and Clayton R. N. (1966) Oxygen-isotope fractionations in systems containing dolomite. *J. Geol.* **74**, 174-196.
- Schauble E. A., Ghosh P. and Eiler J. M. (2006) Preferential formation of C-13-O-18 bonds in carbonate minerals, estimated using first-principles lattice dynamics. *Geochim. Cosmochim. Acta* **70**, 2510-2529. doi:10.1016/j.gca.2006.02.011
- Schmidt M., Xeflide S., Botz R. and Mann S. (2005) Oxygen isotope fractionation during synthesis of CaMg carbonate and implications for sedimentary dolomite formation. *Geochim. Cosmochim. Acta* **69**, 4665-4674.
- Sharp Z.D. and Kirschner D. L. (1994) Quartz-calcite oxygen-isotope thermometry - A calibration based on natural isotopic variations. *Geochim. Cosmochim. Acta* **58**, 4491-4501. doi:10.1016/0016-7037(94)90350-6

Sheppard S. M. and Schwarz H. P. (1970) Fractionation of carbon and oxygen isotopes and magnesium between coexisting metamorphic calcite and dolomite. *Contrib. Mineral. Petr.* **26**, 161-198. doi:10.1007/bf00373200

Streit E., Kelemen P. and Eiler J. (2012) Coexisting serpentine and quartz from carbonate-bearing serpentized peridotite in the Samail Ophiolite, Oman. *Contrib. Mineral. Petr.* **164**, 821-837. doi:10.1007/s00410-012-0775-z

Vasconcelos C., McKenzie J. A., Warthmann R. and Bernasconi S. M. (2005) Calibration of the d18O paleothermometer for dolomite precipitated in microbial cultures and natural environments. *Geology* **33**, 317-320.

Supplemental Tables and Figures

Supplementary Tables

The following Supplementary Tables can be downloaded in a single Excel file in the online version of this article:

Supplementary Table S1. Sample locations and descriptions

Supplementary Table S2. Detailed clumped isotope data

Supplementary Table S3. Empirical transfer function for clumped isotope data

Supplementary Table S4. Bulk rock compositions by XRF

Supplementary Table S5. Quartz $\delta^{18}\text{O}$

Supplementary Table S6. Carbonate oxygen isotope thermometry

Supplementary Table S7. Average electron microprobe analyses of carbonate

Supplementary Table S8. Average electron microprobe analyses of sheet silicate

Supplementary Table S9. Average electron microprobe analyses of relict olivine

Supplementary Table S10. Average electron microprobe analyses of iron oxides and hydroxides

Supplementary Table S11. Average electron microprobe analyses of spinels

Supplementary Table S12. Average electron microprobe analyses of miscellaneous minor and trace minerals

Supplementary Table S13. Bulk Sr isotopic data

Supplementary Table S14. Rb-Sr data isochron data

Supplementary Figures

Supplementary Figure captions and Supplementary Figures S1-S8 follow below.

Supplementary Figure Captions

Figure S1. Zoned soapstone reaction fronts in Wadi Abyad, (a) in outcrop (pen for scale) and (b) in thin section.

Figure S2. Fe# (molar Fe/(molar Fe + Mg)) histograms for serpentine, talc, and magnesite in low-temperature carbonate-veined serpentinite (carb-serp), listvenite and samples from the listvenite-serpentinite transition zone in Wadi Mansah (listvenite, listv-trans), and soapstone from Wadi Abyad (soapstone), compared with olivine analyses (olivine, n = 91) from partially serpentinized peridotite associated with these carbonated lithologies.

Figure S3. Partially serpentinized peridotite with high-Fe serpentine around olivine relicts in sample OM10-06, a partially serpentinized peridotite sample from near the margin of the listvenite at Wadi Mansah, shown in (a) back-scattered electron image, WDS elemental maps of (b) Fe and (c) Si, and (d) EDS elemental map of Si. Fe-rich serpentine is interpreted to post-date mesh texture veinlets and to have formed as a product of low-temperature serpentinization as observed elsewhere (Streit et al., 2012; Evans et al., 2009).

Figure S4. $\Delta 47$ of magnesites formed at known temperatures compared with published carbonate clumped isotope calibrations, projected into the absolute reference frame of Dennis et al. (2011). Y-error bars represent one standard deviation; x-error bars represent reported temperature range. Three magnesite samples were plotted separately (red x's)

because of high temperatures of formation exceeding likely closure temperatures, uncertain temperature of formation, or uncertain mineralogy (see Supplementary section S.2 for discussion).

Figure S5. Examples of modified volatile-free isocon diagrams for some magnesite + quartz listvenites (top, red diamonds) and ambient partially serpentinized peridotite (bottom, green triangles) with compositions near average Oman harzburgite. X axes are re-scaled, volatile-free element concentrations in the protolith (average Oman harzburgite (Hanghøj et al., 2010)). Y axes are volatile-free element concentrations in altered rocks; error bars represent 2- σ analytical uncertainty. For comparison, average Oman harzburgite compositions are plotted as black dots forming a 1:1 line, with error bars marking the 2- σ natural compositional variability in Oman harzburgite compositions reported by Hanghøj et al. (2010). Element concentrations (and corresponding uncertainties) are scaled for convenience as $50 \times \text{wt\% K}_2\text{O}$, $100 \times \text{wt\% P}_2\text{O}_5$, $100 \times \text{wt\% TiO}_2$, $2.5 \times \text{wt\% CaO}$, $30 \times \text{wt\% MnO}$, $0.3 \times \text{ppm Cu}$, $15 \times \text{wt\% Cr}_2\text{O}_3$, $0.003 \times \text{ppm Ni}$, $10 \times \text{wt\% Al}_2\text{O}_3$, $100 \times \text{wt\% Na}_2\text{O}$, $1 \times \text{ppm Sc}$, $1.5 \times \text{wt\% FeO}^*$, $0.3 \times \text{wt\% SiO}_2$, $0.32 \times \text{wt\% MgO}$.

Figure S6. Fuchsite pseudomorphing Cr-spinel in OM10-26, back-scattered electron image (BSE).

Figure S7. Cr# = molar Cr / (Cr + Al) vs. Mg# = molar Mg / (Mg + Fe) for fuchsite (red squares) from listvenite and spinels (blue diamonds) from listvenite and partially

serpentinized peridotite enclosing listvenite bodies at Wadi Mansah, compared to values in spinels from fresh Oman peridotite (grey-filled squares = Samail Massif (Braun, 2004), grey-filled circles = Wadi Tayin harzburgite, grey-filled triangles = Wadi Tayin dunite) and abyssal peridotites (open circles, (Dick, 1989)) presented in figure 5b of Hanghøj et al. (2010).

Figure S8. Fluid $\delta^{18}\text{O}$ from carbonate and quartz in listvenites versus carbonate $\delta^{18}\text{O}$ at temperatures of 80-130°C. Blue squares = dolomite, red diamonds = magnesite, purple circles = quartz. Open symbols represent $\delta^{18}\text{O}$ of the fluid calculated from mineral-water $\delta^{18}\text{O}$ fractionation factors at a temperature of 80°C, filled symbols at 130°C. The range of fluid $\delta^{18}\text{O}$ shown for a single sample and temperature represents the variability in available fractionation factors (top to bottom): Dol - Schauble et al. (2006), Chacko and Deines (2008), Vasconcelos et al. (2005), Northrop and Clayton (1966), Schmidt et al. (2005); Mgs - Aharon (1988) magnesite (1), Aharon (1988) magnesite (2), Schauble et al. (2006), Chacko and Deines (2008); Qtz - Friedman and O'Neil (1977), Sharp and Kirschner (1994). Carbonate and quartz can be considered to be isotopic equilibrium where calculated fluid oxygen isotope values at a given temperature overlap for some choice of fractionation factors for carbonate and quartz. Oxygen isotopes in magnesite and quartz are in good agreement for most choices of fractionation factors for all samples. In dolomite listvenites, quartz and dolomite appear to be in isotopic equilibrium for some choices of fractionation factors in two out of four samples.

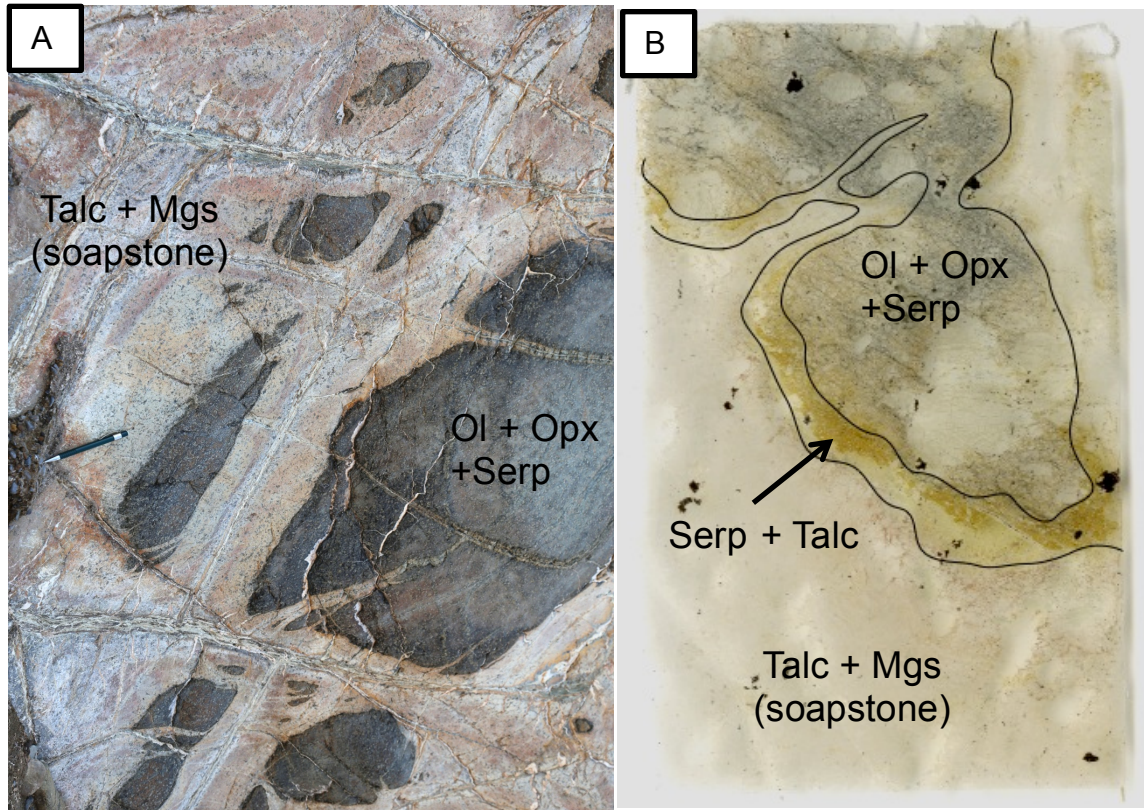


Figure S1

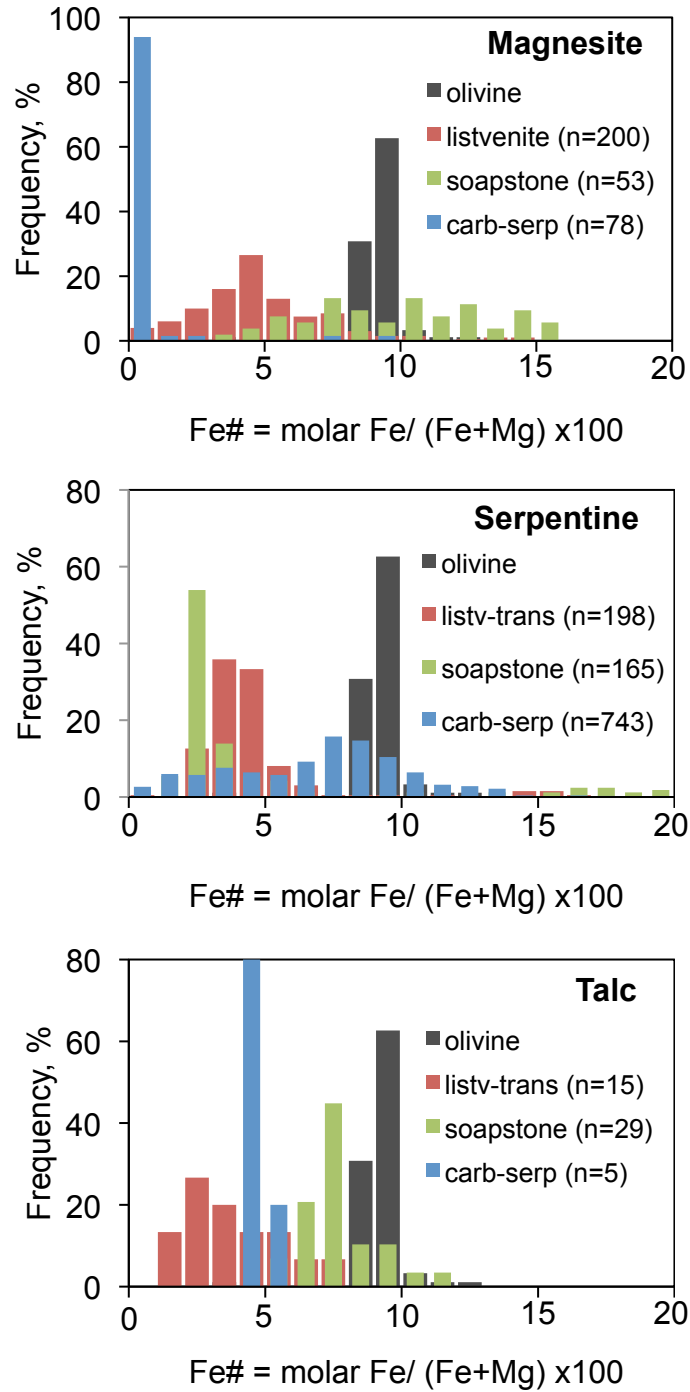


Figure S2

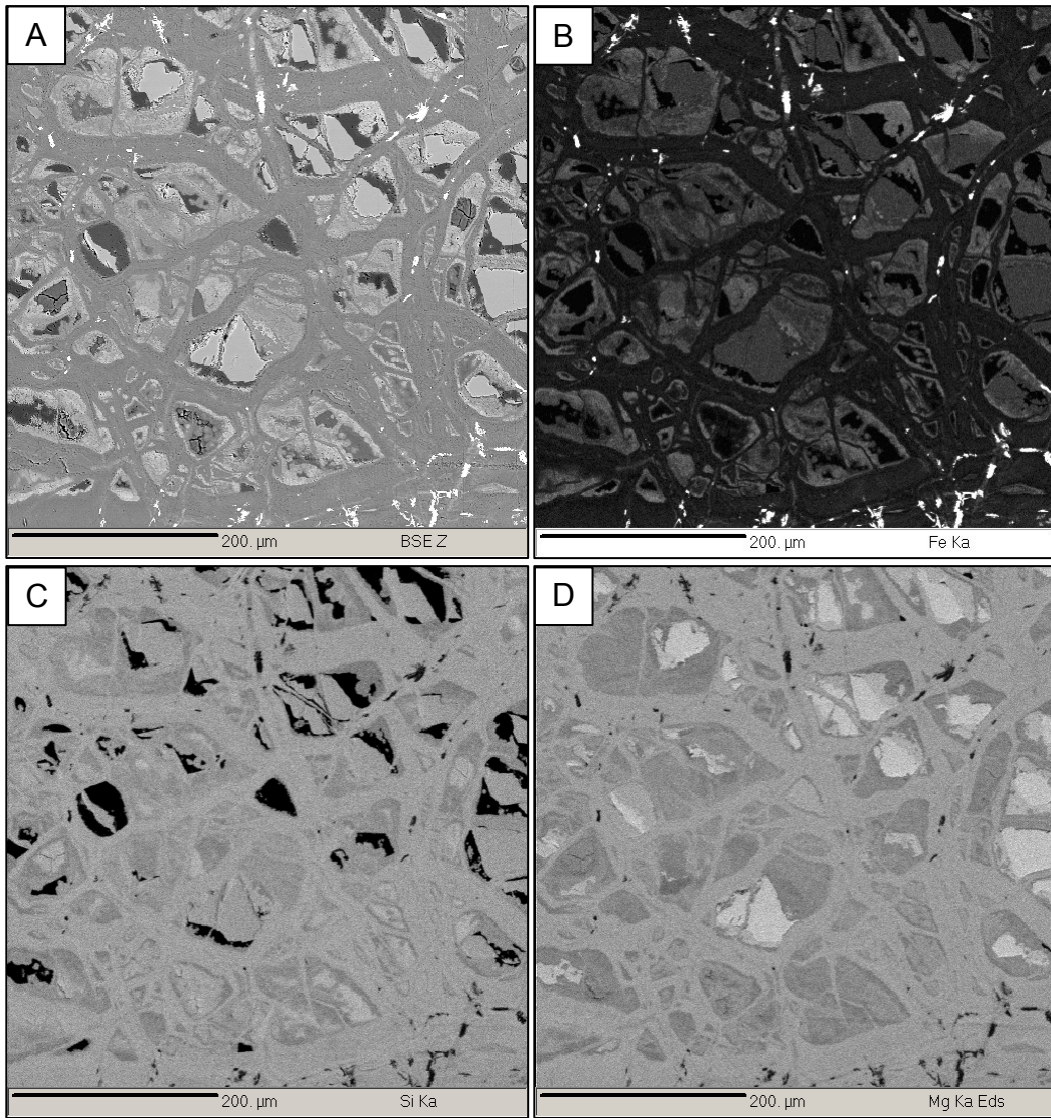


Figure S3

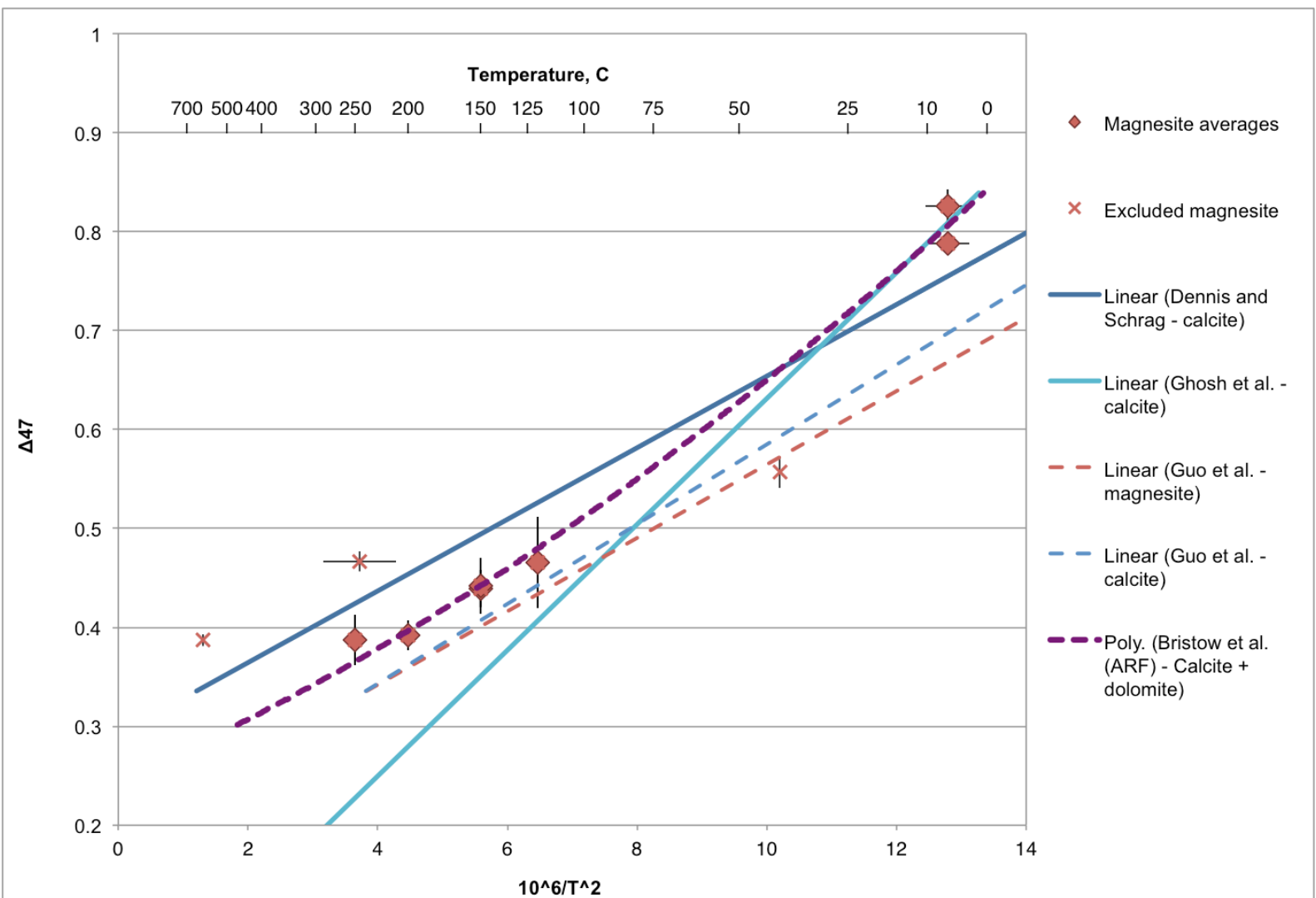
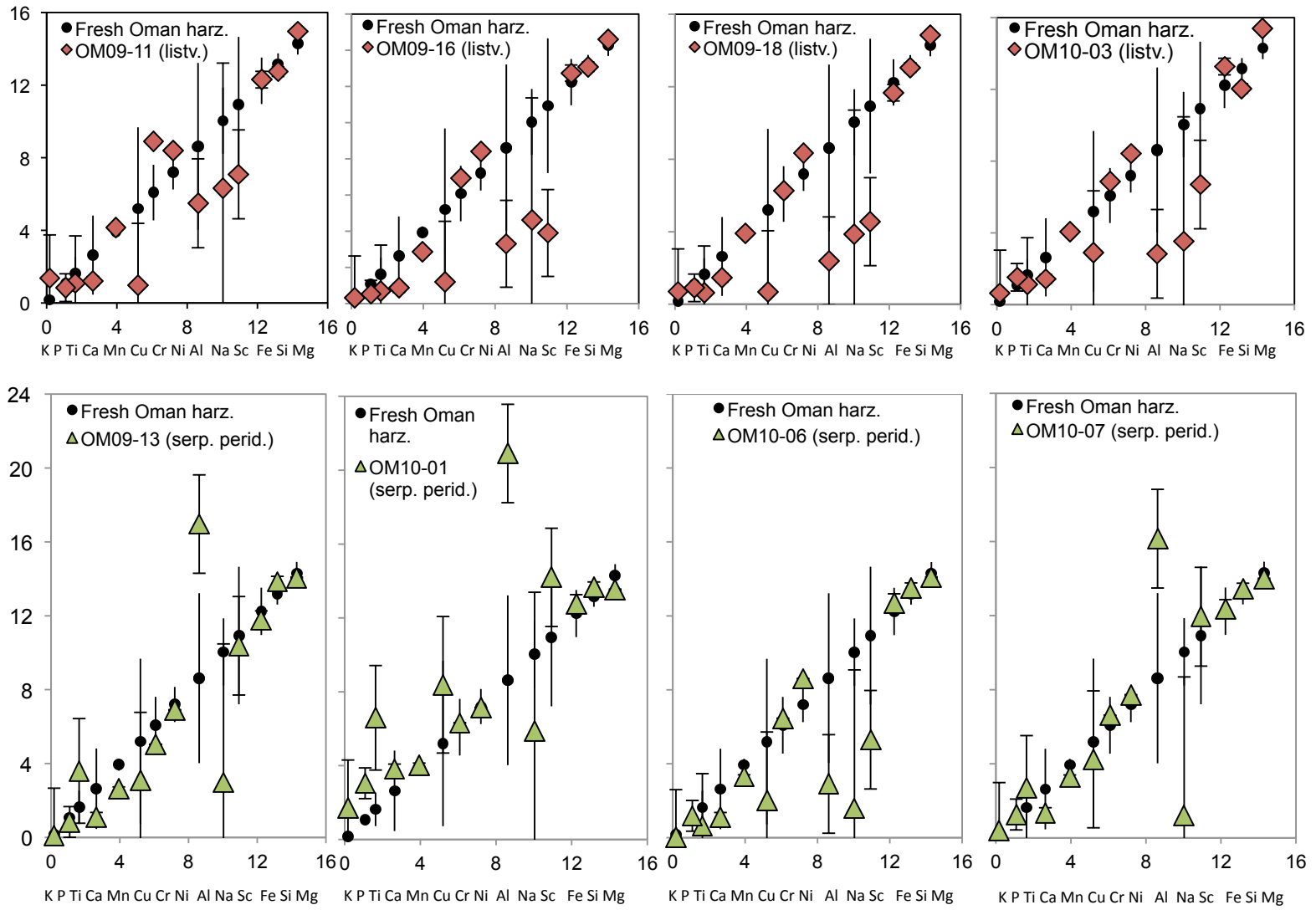


Figure S5



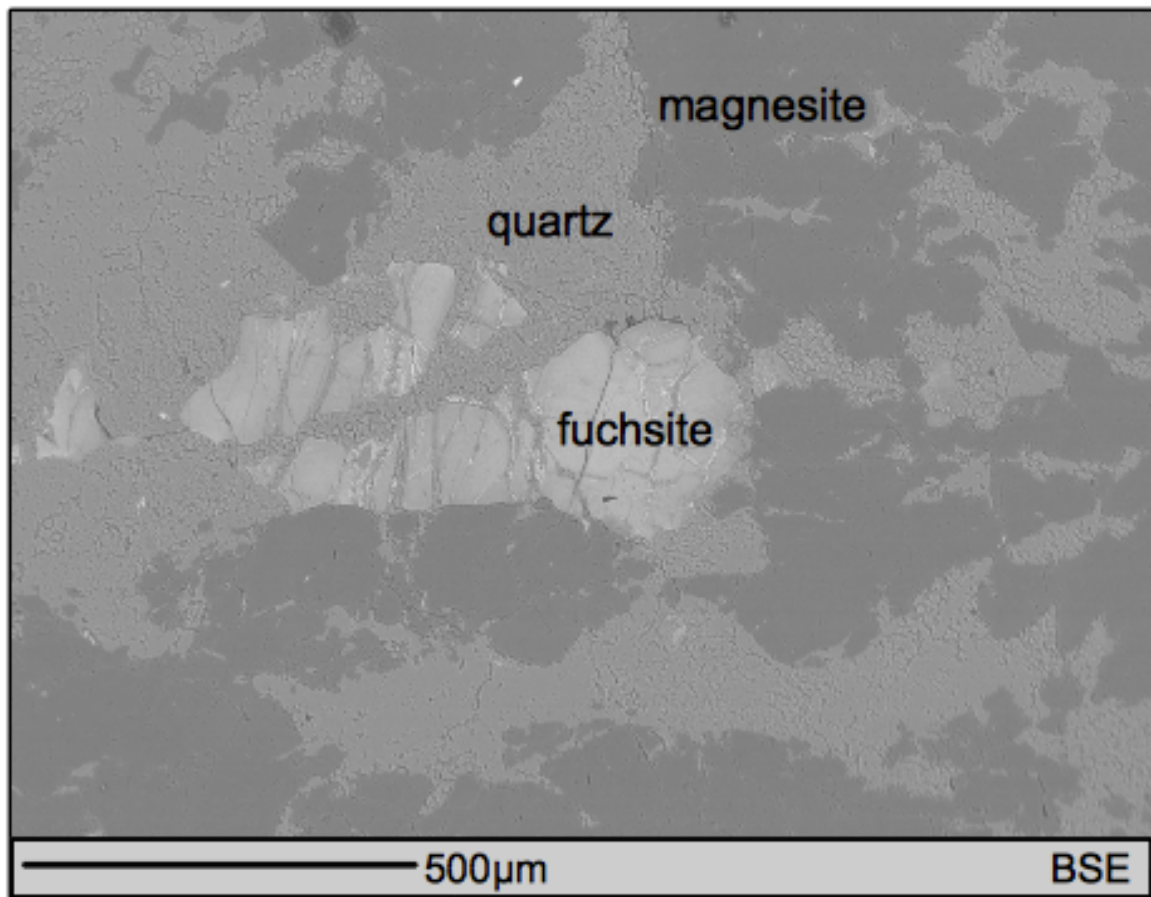


Figure S6

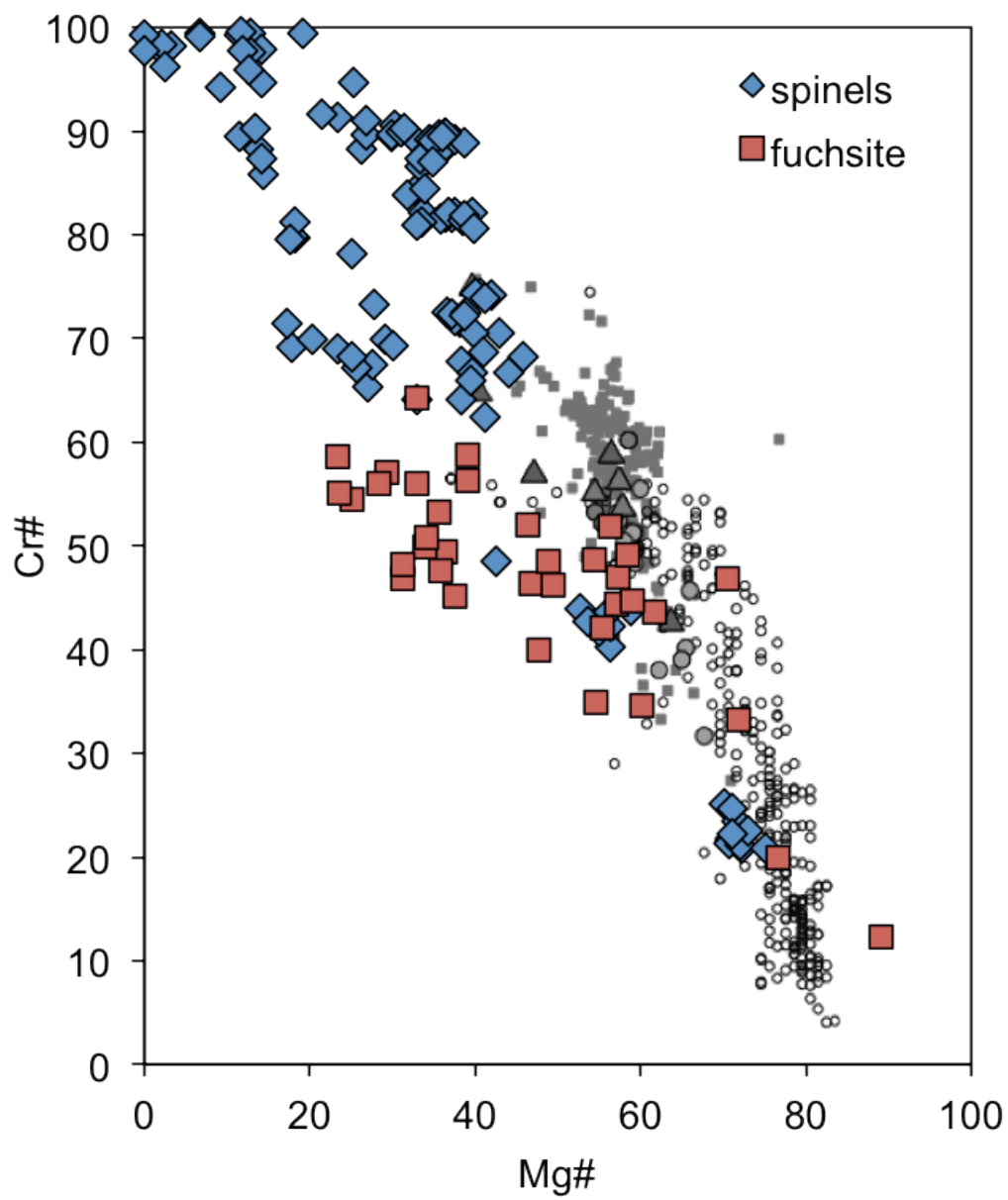


Figure S7

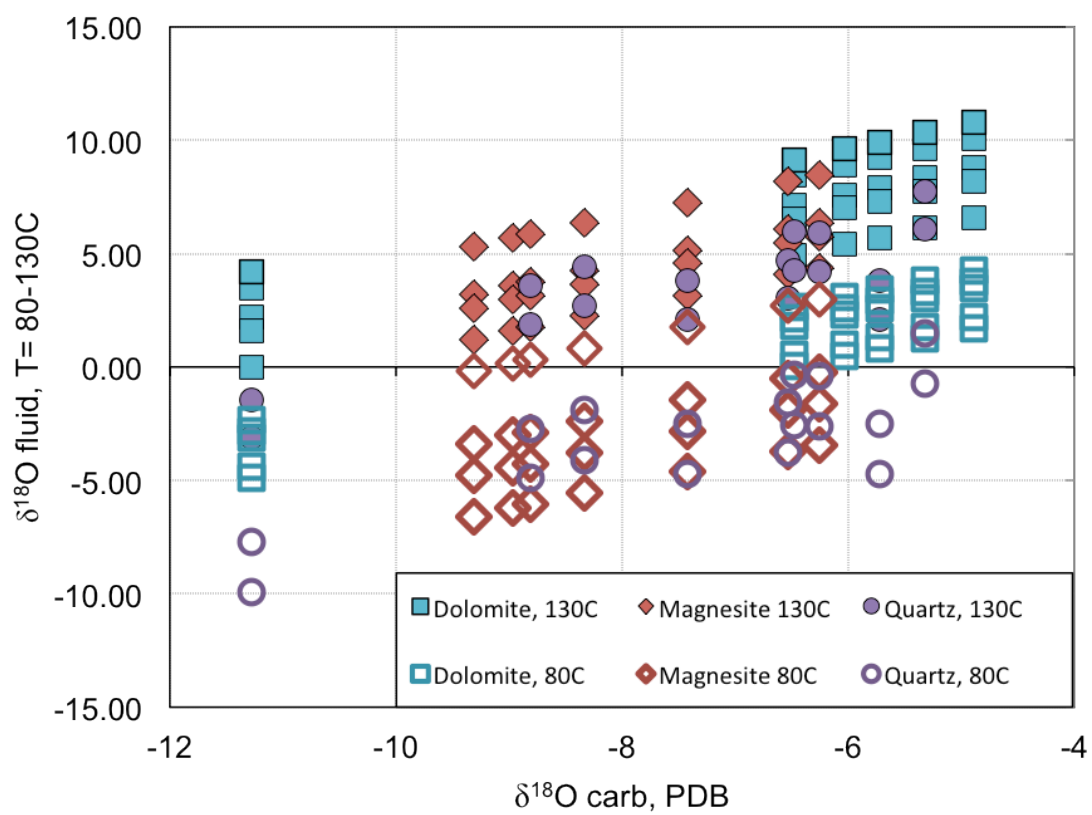


Figure S8